

ADA035340

12

6

# EXCIMER LASERS

A.J. Palmer and L.D. Hess

Hughes Research Laboratories  
3011 Malibu Canyon Road  
Malibu, CA 90265

December 1976

Contract N00014-75-C-0081

Final Technical Report

For Period 1 October 1974 through 15 August 1976

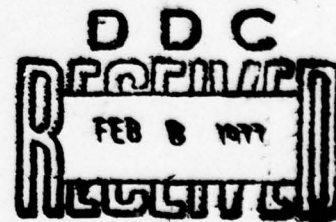
Sponsored By

DEFENSE ADVANCED RESEARCH PROJECTS AGENCY

DARPA Order No. 1807

Monitored By

OFFICE OF NAVAL RESEARCH



DARPA Order No.	1807
Program Code No.	6E20
Contractor	Hughes Research Laboratories
Effective Date of Contract	1 October 1974
Contract Expiration Date	15 August 1976
Amount of Contract	\$259,000.00
Contract No.	N00014-75-C-0081
Principal Investigator	A. Jay Palmer
Telephone No.	(213) 456-6411, extension 356
Title of Work	Excimer Lasers



UNCLASSIFIED

SECURITY CLASSIFICATION OF THIS PAGE (When Data Entered)

REPORT DOCUMENTATION PAGE		READ INSTRUCTIONS BEFORE COMPLETING FORM
1. REPORT NUMBER <i>Final Technical Rept. 1 Oct 74-15 Aug 76</i>	2. GOVT ACCESSION NO.	3. RECIPIENT'S CATALOG NUMBER
4. TITLE (and Subtitle) <b>EXCIMER LASERS.</b>		5. TYPE OF REPORT & PERIOD COVERED Final Tech. Report 1 Oct 1974-15 August 1976
6. AUTHOR <i>A. J. Palmer L.D. Hess</i>		7. PERFORMING ORG. REPORT NUMBER
8. PERFORMING ORGANIZATION NAME AND ADDRESS Hughes Research Laboratories 3011 Malibu Canyon Road Malibu, CA 90265		9. CONTRACT OR GRANT NUMBER(s) <i>N00014-75-C-0081 WARPA Order-1807</i>
10. CONTROLLING OFFICE NAME AND ADDRESS Defense Advanced Research Projects Agcy. Arlington, VA 22209		11. PROGRAM ELEMENT PROJECT TASK AREA & WORK UNIT NUMBERS ARPA Order No. 1807 Program Code No. 6E20
12. MONITORING AGENCY NAME & ADDRESS (if different from Controlling Office) Office of Naval Research 800 N. Quincy Street Arlington VA 22217		12. REPORT DATE <i>Dec 1976</i>
		13. NUMBER OF PAGES 97
		14. SECURITY CLASS. (of this report) <b>UNCLASSIFIED</b>
15. DECLASSIFICATION DOWNGRADING SCHEDULE		
16. DISTRIBUTION STATEMENT (of this Report) <div style="border: 1px solid black; padding: 5px; text-align: center;"><b>DISTRIBUTION STATEMENT A</b> Approved for public release; Distribution Unlimited</div>		
17. DISTRIBUTION STATEMENT (of the abstract entered in Block 20, if different from Report) Approved for public release; distribution unlimited.		
18. SUPPLEMENTARY NOTES		
19. KEY WORDS (Continue on reverse side if necessary and identify by block number) Excimer Lasers, Dimer Lasers, Alkali-Rare Gas Lasers, Continuum Lasers		
20. ABSTRACT (Continue on reverse side if necessary and identify by block number) The results of a theoretical and experimental program addressed to demonstrating the feasibility of a high-energy alkali-rare gas excimer/dimer laser are reported. The major theoretical accomplishments are the development of a detailed model for flashlamp pumping of all the alkali-xenon excimer/dimer systems and for discharge pumping of the potassium-xenon and potassium-argon systems. The models predict that laser oscillation is attainable under practical laboratory		

DD FORM 1 JAN 73 1473 EDITION OF 1 NOV 65 IS OBSOLETE

UNCLASSIFIED

SECURITY CLASSIFICATION OF THIS PAGE (When Data Entered)

142600

JP

DDC  
RECEIVED  
FEB 8 1977  
A

UNCLASSIFIED

SECURITY CLASSIFICATION OF THIS PAGE(When Data Entered)

conditions on both the excimer and dimer bands of these systems. Major accomplishments of the experimental program are a measurement of the stimulated emission coefficient on the K-Xe excimer band during flashlamp pumping which was consistent with the model; the attainment of a 1  $\mu$ sec. pulsed diffuse discharge through an aerosol-free K-Ar mixture under conditions predicted by the model to be sufficient for achieving laser oscillation on the excimer and dimer bands and the attainment of preliminary absolute fluorescence data on the discharge pumped K-Ar excimer band indicative of a resonance level concentration within an order of magnitude of that predicted by the model.

microsec.

UNCLASSIFIED

SECURITY CLASSIFICATION OF THIS PAGE(When Data Entered)

MISSING PAGE  
NUMBERS ARE BLANK  
AND WERE NOT  
FILMED

# TABLE OF CONTENTS

SECTION		PAGE
	LIST OF ILLUSTRATIONS . . . . .	5
I	INTRODUCTION . . . . .	9
II	OPTICAL PUMPING OF ALKALI-RARE-GAS EXCIMER AND DIMER MOLECULES . . . . .	11
	A. Theoretical Program . . . . .	11
	B. Experimental Program . . . . .	26
III	DISCHARGE PUMPING OF THE ALKALI EXCIMER AND DIMER MOLECULES . . . . .	39
	A. Theoretical Program . . . . .	39
	B. Results and Discussions . . . . .	45
	C. Experimental Program . . . . .	49
IV	CONCLUSIONS AND RECOMMENDATIONS . . . . .	75
V	ALKALI SOURCE STUDIES . . . . .	77
	A. Cesium Chromate Pellets . . . . .	77
	B. Heat Pipe Oven Technique . . . . .	77
	C. Alkali Metal Deposition along the Tube Wall . . . . .	78
	D. Side Arm Evaporation . . . . .	78
	E. Carrier Gas Transport of the Alkali . . . . .	79
	REFERENCES . . . . .	81
	APPENDIX - Computer Programs . . . . .	85

SEARCHED FOR	
CTTS	Write Section <input checked="" type="checkbox"/>
GOO	Diff Section <input type="checkbox"/>
WATERBORNE	<input type="checkbox"/>
CERTIFICATION	
<i>letter on file</i>	
BY	
DISTRIBUTION/AVAILABILITY CODES	
SAC	
MAIL, and/or SPECIAL	
A	



# LIST OF ILLUSTRATIONS

FIGURE		PAGE
II-1	Energy flow diagram for the K-Xe/K <sub>2</sub> system under optical pumping . . . . .	12
II-2	Small-signal gain versus wavelength for the optically pumped alkali xenon excimer/dimer systems . . . . .	24
II-3	Small-signal gain versus wavelength for the optically pumped alkali xenon excimer/dimer systems . . . . .	24
II-4	Early experimental apparatus — flashlamp pumping . . . . .	27
II-5	Potassium-xenon absorption coefficient . . . . .	29
II-6	Potassium-xenon absorption coefficient . . . . .	30
II-7	Final optical pumping apparatus . . . . .	31
II-8	Photograph of final optical pumping apparatus . . . . .	32
II-9	Flashlamp output measurements . . . . .	34
II-10	Theoretical small signal gain coefficient versus wavelength . . . . .	35
II-11	Gain measurement: 8220 Å . . . . .	37
II-12	Gain measurement: 6329 Å . . . . .	37
III-1	Theoretical modeling results for avalanche sustained discharge pumping of the K-Xe/K <sub>2</sub> system . . . . .	46
III-2	Theoretical modeling results for uv sustained discharge pumping of the K-Xe/K <sub>2</sub> system . . . . .	47
III-3	Theoretical modeling results for avalanche sustained discharge pumping of K-Ar system under conditions achieved in early discharge experiments . . . . .	48

FIGURE		PAGE
III-4	Alkali-rare-gas discharge tube, design 1 . . . . .	51
III-5	Photograph of alkali-rare-gas high- pressure discharge apparatus, design 2 . . . . .	53
III-6	Photograph of alkali-rare-gas discharge apparatus, design 3 . . . . .	53
III-7	Schematic of alkali-rare-gas discharge apparatus and optical monitoring equipment . . . . .	54
III-8	Optical transmission data illustrating aerosol formation in potassium-argon mixture . . . . .	55
III-9	Schematic of apparatus for optical measurements of alkali-rare-gas mixture with uniform temperature control . . . . .	57
III-10	Potassium dimer spectra . . . . .	58
III-11	Optical transmission through potassium- argon in a 15 cm sealed-off cell . . . . .	60
III-12	Optical transmission through the discharge apparatus . . . . .	62
III-13	Experimental and calculated optical transmission data for the configuration shown in Figure III-4 . . . . .	63
III-14	Photograph of potassium-argon discharge as viewed through the 1.5 cm side window . . . . .	65
III-15	Current-voltage waveform characteristics of potassium-argon transverse discharge . . . . .	66
III-16	Current voltage characteristics of potassium-argon discharge . . . . .	67
III-17	Potassium-argon excimer emission . . . . .	68

FIGURE		PAGE
III-18	Temporal profiles of potassium-argon excimer emission and discharge current . . . . .	70
III-19	Superposition of potassium-argon excimer optical emission and transmission spectra . . . . .	70



## I. INTRODUCTION

The A-to-X transition on the diatomic alkali-rare-gas molecules (excimers) and the alkali dimer molecules has been recognized for some time as a potentially efficient high-average-power tunable laser transition.<sup>1,2</sup> At a rare-gas pressure on the order of 10 atm and an alkali partial pressure of a fraction of a Torr, both the dimer (for the heavier alkalis) and the excimer transitions are continuum transitions, each roughly 1000 Å wide, lying in the visible to near-infrared portions of the spectrum.

The primary goals of this program were to identify specific operating conditions for achieving laser oscillation on the A-to-X transitions of the diatomic alkali-rare-gas molecules (excimers) and of the diatomic homonuclear alkali molecules (dimers), and to demonstrate net laser gain in a laboratory experiment from at least one of the alkali-rare-gas systems. The primary accomplishments of the program in rough chronological order are:

- (1) The development of a theoretical model which computes the small-signal gain for all of the alkali-xenon excimer/dimer systems for flash-lamp optical pumping.<sup>3</sup>
- (2) The construction of a one meter long, high-temperature, high-pressure optically pumped potassium xenon experimental cell.
- (3) Experimental measurements of the absorption coefficient on the K-Xe and K-Ar excimer and K<sub>2</sub> dimer band and of the stimulated emission coefficient on the K-Xe excimer band; all these measurements were consistent with the modeling.<sup>4</sup>
- (4) Observations of low-pressure discharge pumped fluorescence spectra of the K-Ar excimer and dimer bands.



- (5) The development of a completely time-dependent theoretical model for discharge pumping of the K-Xe and K-Ar excimer/dimer systems.
- (6) The construction of a transverse discharge apparatus utilizing a 1 x 2 x 13.5 cm discharge volume and a flashlamp preionizer.
- (7) The achievement of aerosol-free equilibrium potassium vapor pressures at temperatures up to 325°C and argon pressures up to 10 atm in the transverse discharge system.
- (8) The attainment of a diffuse transverse discharge through a K-Ar mixture under the conditions of No. 7 at a current density level sufficient (according to the model) to reach lasing threshold on both the K-Ar excimer and K<sub>2</sub> dimer bands.
- (9) Measurements of the absorption and fluorescence spectrum of the K-Ar excimer and K<sub>2</sub> dimer bands under the above discharge conditions, and preliminary quantitative evaluation of fluorescence power and laser gain.

The first year of the program was devoted to the theory of and experiments in optical pumping of the K-Xe excimer/dimer system; that material is covered in Section II. The second year was devoted to discharge pumping of the potassium system; this is discussed in Section III. Section IV covers our study of alternative alkali sources for use in alkali-rare-gas lasers. Section V summarizes the results of the program and presents conclusions and recommendations for further study.

## II. OPTICAL PUMPING OF ALKALI-RARE-GAS EXCIMER AND DIMER MOLECULES

### A. Theoretical Program

In this section, we show theoretically that both the alkali-xenon excimer and the alkali dimer transitions can exhibit practical laser gain for broadband optical pumping with flashlamps. We discuss the physics of the gas-kinetic and optical processes involved in this pumping scheme and we present results for the predicted small-signal gain versus wavelength for all of the alkali-xenon excimer and dimer systems for a chosen practical set of operating conditions.

#### 1. Model Physics

Resonance lamp optical pumping of the alkali resonance level in an alkali-rare-gas mixture has, in the past, been used to produce alkali-rare-gas excimer species to study the excimer level fluorescence spectra.<sup>5</sup> Although this technique is well suited for interpretation of the fluorescence spectra, it cannot be used to achieve dimensionally scalable laser pumping due to the extremely short penetration depth of the resonance line through the alkali densities required for achieving practical laser gain coefficients on the excimer and dimer transitions.<sup>6</sup> A more practical pumping scheme for this purpose is to pump with a broadband source such as a xenon flashlamp into the absorption bands arising from the excimer and dimer transitions themselves. The pumping kinetics are only slightly more involved than those associated with resonance line pumping. An energy flow diagram for this type of pumping is shown in Figure II-1 for the K-Xe/K<sub>2</sub> system. We proceed now to discuss the various approximations used in modeling the physics of this pumping scheme.

First, the pump source spectra will, in general, extend into the visible and ultraviolet portions of the spectrum. Thus, there will be some added contribution to the A-state pumping from radiative decay of upper levels into the A states; these processes are neglected as a conservative approximation for the laser gains.

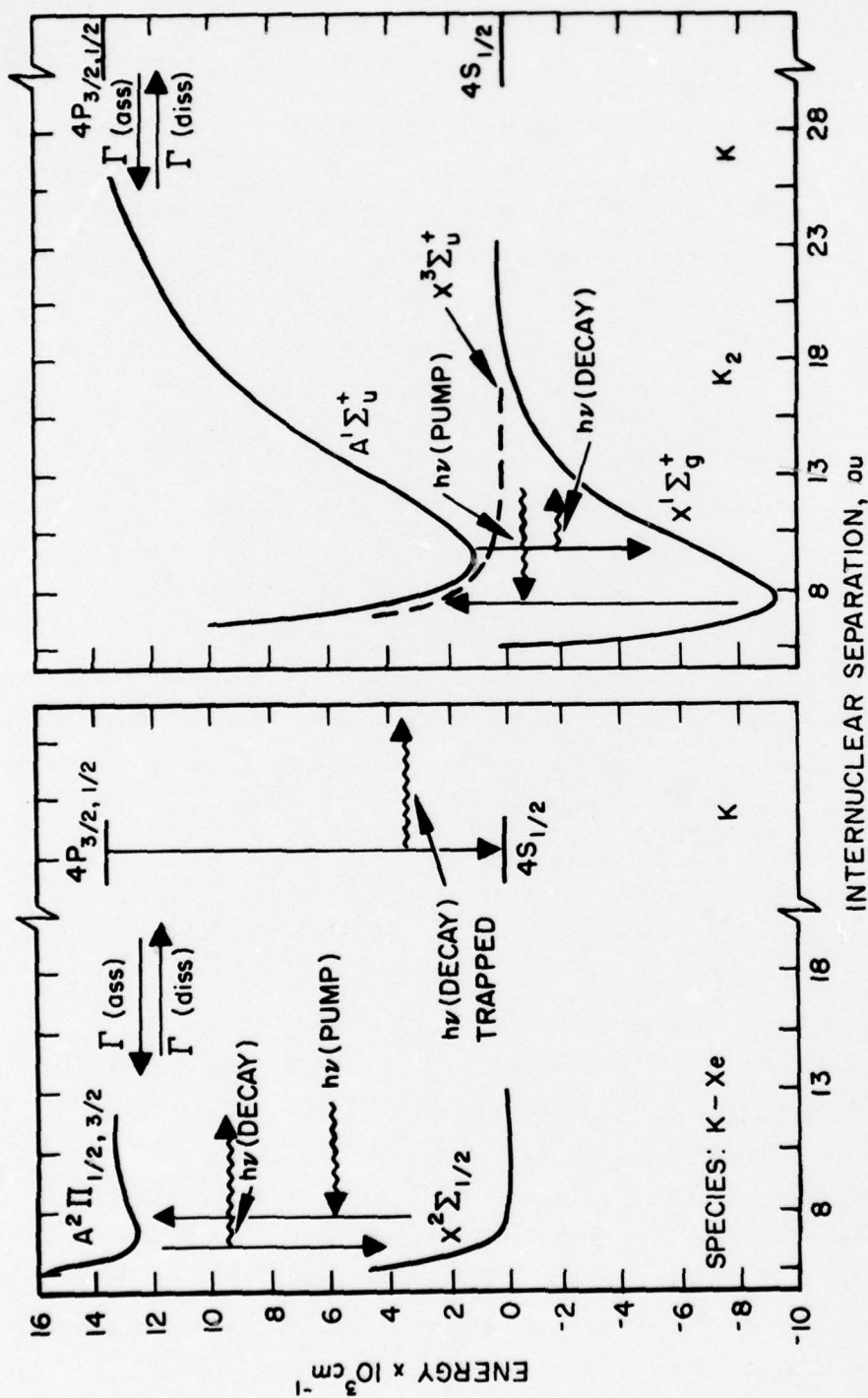


Figure II-1. Energy flow diagram for the K-Xe/ $K_2$  system under optical pumping.



Another possible involvement of higher electronic states is the possible contribution to absorption at the laser wavelengths caused by photoexcitation of the A states into these states. This has been termed "self-absorption" and has led to serious reduction or elimination of net laser gain in other excimer systems.<sup>7,8</sup> In the case of the alkali-xenon A-X excimer transition, it can be seen from an inspection of calculated upper-state potential energy curves of Ref. 9 that there are no allowed transitions which could lead to serious self-absorption. The situation with the dimers is less certain, owing to a lack of knowledge of the higher-level potential energy curves. It appears unlikely that transitions to appropriately positioned upper-level curves will be present with an oscillator strength strong enough to compete with the strong A-X transition over the full laser bandwidth, and we will assume for simplicity that such transitions are not present.

The only other electronic states which could possibly interfere with laser kinetics are the dimer bound  $a^3\Pi_u$  and repulsive  $x^3\Sigma_u$  triplet states which lie below the dimer A state. If the  $a^3\Pi_u$  state is strongly coupled to the A state (for example, through spin-orbit interaction in collisions with xenon atoms) and if the bound portion of the  $a^3\Pi_u$  state either crosses or is in close proximity with the repulsive  $x^3\Sigma_u$  state, then predissociation could cause rapid depletion of the A state. This point is discussed in detail in Ref. 4 with fairly strong arguments presented that predissociation will probably not occur at least for the  $K_2$  and  $Na_2$  cases. For these computations, we assume that the triplet states do not enter importantly into the laser kinetics except, of course, in their contribution to the A-state statistical weights. Considering the high pressures dealt with, this is probably the most suspect assumption made and calls for experimental or theoretical resolution. The observed strong fluorescence of the A states of all of the alkali dimers (except  $Li_2$ , which was not studied)<sup>10</sup> at alkali pressures up to 1 Torr provides evidence that predissociation is not a problem at low pressures.



Concerning vibrational levels, the vibrational level spacing for the bound alkali excimer and dimer states is, except for  $\text{Li}_2$  and  $\text{Na}_2$ , small compared to  $kT$ . Therefore, at the pressures of interest here, individual vibrational transitions are broadened into one another and the band spectrum is essentially a continuum. The assumption of a continuous band for  $\text{Li}_2$  and  $\text{Na}_2$  is made in the modeling and will represent a conservative approximation for the laser gain results, since the actual gain should show peaks higher than the continuum level at the discrete vibrational modes. Under these conditions, it is appropriate to partition the bound as well as the unbound electronic states into a continuum set of substates characterized by their internuclear separation and populated according to a classical canonical ensemble.<sup>5</sup> Such an equilibrium distribution among the substates within a given electronic state will always maintain under our considered operating conditions, since collisional relaxation among the substates is mediated by binary collision at a rate which is fast compared to radiative decay rates or pumping rates. On the other hand, relaxation between the bound substates and their free dissociation products must be mediated by three-body collisions which, for the dimer A state, will not always occur at rates which dominate over radiative decay rates (as will be seen below). Therefore, equilibrium with respect to the dissociation products is not assumed a priori.

In the model there are then six electronic state species participating in the A-X excimer and dimer laser kinetics. They are ground-state alkali-xenon molecules  $[\text{XEx}]$ , A-state alkali-xenon excimer molecules  $[\text{AEx}]$ , ground-state alkali dimer molecules  $[\text{XD}i]$ , A-state alkali dimer molecules  $[\text{AD}i]$ , unbound resonance-state alkali atoms  $[\text{alk}^*]$ , unbound ground-state alkali atoms  $[\text{alk}]$ , and unbound ground-state xenon atoms  $[\text{Xe}]$ . In terms of the subelectronic-state concentrations, the expression for the net small-signal gain due to both excimers and dimers is<sup>1,2</sup>

$$\begin{aligned} \text{gain} = & \frac{\lambda^2}{8\pi} A \left[ \frac{d[A_{Ex}]}{dR} - \left( \frac{g_{A_{Ex}}}{g_{X_{Ex}}} \right) \frac{d[X_{Ex}]}{dR} \right] \frac{dR}{d\nu} \Big|_{Ex} \\ & + \frac{\lambda^2}{8\pi} A \left[ \frac{d[A_{Di}]}{dR} - \left( \frac{g_{A_{Di}}}{g_{X_{Di}}} \right) \frac{d[X_{Di}]}{dR} \right] \frac{dR}{d\nu} \Big|_{Di} , \quad (\text{II-1}) \end{aligned}$$

where  $d[ ]$  represents the substate concentrations for an internuclear separation between  $R$  and  $R + dR$ ,  $A$  is the Einstein coefficient for the transition (assumed independent of  $R$ ),  $\lambda$  and  $\nu$  are the wavelength and frequency of the radiation, and the  $g$  factors are the degeneracy factors for the electronic states indicated.

The molecular ground-state concentrations are assumed to remain in equilibrium with that of their dissociation products since the production and loss rates for these species, under our considered operating conditions, are dominated by gas-kinetic processes. Thus, for the ground-state species, we can write, according to classical statistics,<sup>5</sup> the substate population at an internuclear separation between  $R$  and  $R + dR$  as<sup>1,2</sup>

$$d[X_{Ex}] = 4\pi R^2 dR \left( g_{X_{Ex}} / g_{X_{Ex},f} \right) \exp \left( -W_{X_{Ex}}(R) / kT \right) [alk] [Xe] , \quad (\text{II-2})$$

$$d[X_{Di}] = 4\pi R^2 dR \left( g_{X_{Di}} / g_{X_{Di},f} \right) \exp \left( -W_{X_{Di}}(R) / kT \right) [alk]^2 . \quad (\text{II-3})$$

Here [ ] indicates species concentration, and  $g_x$  and  $g_f$  are the degeneracies of the molecular X state and its parent atomic state, respectively.  $WX(R)$  is the energy of the molecular substate relative to that of its parent atomic state,  $k$  is Boltzmann's constant, and  $T$  is gas temperature.

The absorption coefficient due to X-A transitions can, therefore, be written immediately as<sup>1,2,5</sup>

$$\beta_{Ex} = \frac{\lambda^2}{2} \frac{AR^2}{dv/dR} \exp\left(-\frac{WX_{Ex}(R)}{kT}\right) \left(\frac{g_{X_{Ex}}}{g_{X_{Ex,f}}}\right) \times [alk][Xe], \quad (II-4)$$

$$\beta_{Di} = \frac{\lambda^2}{2} \frac{AR^2}{dv/dR} \exp\left(-\frac{WX_{Di}(R)}{kT}\right) \left(\frac{g_{X_{Di}}}{g_{X_{Di,f}}}\right) [alk]^2 \quad . \quad (II-5)$$

The three excited-state populations are governed by the following steady-state rate equations:

$$\begin{aligned} \frac{d}{dt}[alk^*] &= R_{Ex,f} + R_{Di,f} + \Gamma_{diss,Ex}[A_{Ex}] + \Gamma_{diss,Di}[A_{Di}] \\ &- (\Gamma_{ass,Ex} + \Gamma_{ass,Di} + \Gamma_{rad,alk^*})[alk^*] = 0 \quad , \quad (II-6) \end{aligned}$$

$$\begin{aligned} \frac{d}{dt}[A_{Ex}] &= R_{Ex,b} + \Gamma_{ass,Ex}[alk^*] \\ &- (\Gamma_{diss,Ex} + \Gamma_{rad,Ex})[A_{Ex}] = 0 \quad , \quad (II-7) \end{aligned}$$



$$\frac{d}{dt} [A_{Di}] = R_{Di,b} + \Gamma_{ass,Di} [alk^*] - \left( \Gamma_{diss,Di} + \Gamma_{rad,Di} \right) [A_{Di}] = 0 \quad (II-8)$$

Here  $R_{Ex,f}$  and  $R_{Di,f}$  are the optical pumping rates on the excimer and dimer transitions, respectively, which lead directly to free  $alk^*$ .  $R_{Ex,b}$  and  $R_{Di,b}$  are the corresponding pumping rates leading directly to bound A-state excimers and dimers, respectively.  $\Gamma_{ass}$  and  $\Gamma_{diss}$  denote the A-state association and dissociation rates and  $\Gamma_{rad}$  denotes the effective radiative decay rate of the state indicated and includes the effects of radiation trapping.

Exchange reactions of the type



and



are excluded from the rate equations since their reaction rates cannot compete with the appropriate radiative or three-body association rates under the operating conditions of interest.

The A-state association and dissociation rates  $\Gamma_{ass}$  and  $\Gamma_{diss}$  can be related through detailed balancing:

$$\Gamma_{ass_{Ex}} / \Gamma_{diss_{Ex}} = K_{A_{Ex}} [Xe] \quad , \quad (II-9)$$

$$\Gamma_{ass_{Di}} / \Gamma_{diss_{Di}} = K_{A_{Di}} [alk] \quad , \quad (II-10)$$



where  $K_{A_{Ex}, D_i}$  is the equilibrium constant for the A-state dissociation-association reaction.

The association rate constant for the excimer A state is on the order of  $10^{-32} \text{ cm}^6 \text{ sec}^{-1}$  for all of the alkali-xenon systems and the A-state equilibrium constant is on the order of  $10^{-22} \text{ cm}^3$  for our temperature ranges of interest.<sup>2, 11</sup> Using Eq. (II-9), one can see that for our xenon concentration of interest ( $[Xe] \sim 10^{20} - 10^{21} \text{ cm}^{-3}$ ), we have

$$\left( \Gamma_{\text{diss}_{Ex}} \approx 10^{10} - 10^{11} \text{ sec}^{-1} \right) \gg \left( \Gamma_{\text{rad}_{Ex}} \approx 10^{+7} \text{ sec}^{-1} \right) \quad (\text{II-11})$$

and

$$\Gamma_{\text{ass}_{Ex}} [\text{alk}^*] \gtrsim \Gamma_{\text{ass}_{Ex}} \left( \frac{R_{Ex, b}}{A} \right) \gg R_{Ex, b} \quad (\text{II-12})$$

By using these conditions in Eq. (II-7), one concludes that bound- as well as free-state excimers will remain in thermal equilibrium with the free-alkali resonance-state population. In this case we can write an expression for the A-state concentration of the same form as Eq. (II-1) for the X-state concentration:

$$d[A_{Ex}] = 4\pi R^2 dR \left( g_{A_{Ex}} / g_{A_{Ex, f}} \right) \exp \left( -W A_{Ex}(R) / kT \right) [\text{alk}^*] [Xe] \quad (\text{II-13})$$

This expression is used in Eq. (II-1) for the gain coefficient and in Eq. (II-20) below.

Similar considerations applied to the coefficients in Eq. (II-8) for dimer A-state concentration reveal that thermal equilibrium between the bound-dimer A-state concentration and that of the alkali resonance level will not always obtain under the operating conditions considered, and we must, in general, write for the steady-state dimer A-state concentration

$$[A_{Di}] = \frac{R_{Di,b} + \Gamma_{ass,Di} [alk^*]}{\Gamma_{diss,Di} + A} \quad (II-14)$$

Here we have put  $\Gamma_{rad,Di} \approx A$  since most of the dimer states radiate at wavelengths where the mixture is transparent in the transverse dimension.

Binary collisions will still maintain the thermal equilibrium within the dimer A state and we can write for the substate population,<sup>4</sup>

$$d[A_{Di}] = 4\pi R^2 dR \exp\left(-W_{A_{Di}}(T)/kT\right) \left(g_{A_{Di}}/g_{A_{Di,f}}\right) \times [A_{Di}]/K_{A_{Di}} \quad (II-15)$$

In Eq. (II-1), for the gain coefficient, the substate concentration  $d[A(R)]$  refers to the total bound plus free states between  $R$  and  $R + dR$ . Although Eq. (II-13) for the excimer state does represent the total contribution from bound plus free states, expression (II-15) for the dimer states gives only the bound-state contribution. However, the bound-state concentration by far dominates the total contribution to the dimer substates in the  $R$  regions of interest at the temperatures considered here. Equation (II-15) can, therefore, be used for the dimer term in expression (II-1) for the gain coefficient.

It remains to determine the free-alkali resonance-state concentration,  $[\text{alk}^*]$ . For this purpose, substitute Eqs. (II-7) and (II-8) into Eq. (II-6) to obtain

$$\begin{aligned} \frac{d}{dt}[\text{alk}^*] &= R_{\text{Ex}} + R_{\text{Di}} - \Gamma_{\text{rad, alk}^*}[\text{alk}^*] - \Gamma_{\text{rad, Ex}}[A_{\text{Ex}}] - [A_{\text{Di}}] \\ &= 0 \quad , \end{aligned} \quad (\text{II-16})$$

where now  $R_{\text{Ex}} = R_{\text{Ex, f}} + R_{\text{Ex, b}}$  and  $R_{\text{Di}} = R_{\text{Di, f}} + R_{\text{Di, b}}$  refer to the total optical pumping rates on the excimer and dimer transition, respectively, and are given by

$$R_{\text{Ex, Di}} = \int \phi(\nu) \beta_{\text{Ex, Di}}(\nu) \exp\left\{-\left[\beta_{\text{Ex}}(\nu) + \beta_{\text{Di}}(\nu)\right] x\right\} d\nu \quad , \quad (\text{II-17})$$

where  $\phi(\nu)$  is the external photon pumping flux incident on an assumed planar boundary of the medium and  $x$  is the propagation distance of the pump radiation into the medium.

Because the dimer binding is strong compared to  $kT$ , essentially all of the dimer transition optical pumping produces bound- rather than free-state dimers, and we can also put

$$R_{\text{Di, b}} = R_{\text{Di}} \quad (\text{II-18})$$

in Eq. (II-14).

The third and fourth terms on the right-hand side of Eq. (II-16) can be combined to read

$$\Gamma_{\text{rad, alk}^*}[\text{alk}^*] = \Gamma_{\text{rad, Ex}}[A_{\text{Ex}}] = \int_0^{R_{\text{max}}} \left( \frac{d[A_{\text{Ex}}]}{dR} \Gamma(R)_{\text{rad, Ex}} \right) dR \quad , \quad (\text{II-19})$$



where the integral extends only up to an internuclear separation  $R_{\max}$ , defined by

$$\frac{1}{\text{alk}^*} \int_0^{R_{\max}} \left( \frac{d[A_{\text{Ex}}]}{dR} \right) dR = 1, \quad (\text{II-20})$$

to ensure proper counting. Here  $d[A_{\text{Ex}}]/dR$  is given by Eq. (II-13) and  $\Gamma(R)_{\text{rad, Ex}}$  is the radiative decay rate for excimer molecules with internuclear separation between  $R$  and  $R + dR$ . A significant fraction of the excited alkali atoms are in the form of either free or bound excimer states which radiate at wavelengths close to the resonance line where the mixture is opaque in the transverse dimension. These latter states will have a trapped radiative rate which is given by Holstein's formula:<sup>12</sup>

$$\Gamma(R)_{\text{rad, Ex}} = A \frac{1.6}{\beta(R)_{\text{Ex, net}} T \left\{ \pi \ln[\beta(R)_{\text{Ex, net}} T] \right\}^{1/2}}, \quad (\text{II-21})$$

where  $T$  is the transverse dimension of the mixture and  $\beta(R)_{\text{Ex, net}}$  is the net absorption coefficient for radiation emitted by the states  $d[A_{\text{Ex}}](R)$ . To a close approximation, it is given by Eq. (II-4), i. e.,  $\beta(R)_{\text{Ex, net}} \approx \beta(R)_{\text{Ex}}$ .

Once the A-state and X-state potential energy curves and the appropriate rate constants have been specified, expressions (II-1) - (II-21) can be combined to compute the net small-signal gain vs wavelength from the A-X excimer and dimer transitions for given values of pumping flux, xenon concentration, alkali concentration, and gas temperature.

The latter two variables are, of course, related. We assume in the model that the alkali vapor is in equilibrium with its condensate at the gas temperature. The ground-state alkali concentration can then be written as a function of temperature according to the phenomenological expression<sup>13</sup>

$$[\text{alk}](\text{cm}^{-3}) = 2.7 \times 10^{16} (273/T) \times 10^{(S_b - 0.052S_a/T)}, \quad (\text{II-22})$$

where T is in  $^{\circ}\text{K}$  and  $S_a$  and  $S_b$  are constants specific to the alkali.

## 2. Results and Discussions

In the computations, the alkali-xenon A-state and X-state potential energy curves are taken from the theoretical curves computed by Pascale and Vandeplanque.<sup>9</sup> An exception is the Li-Xe A state, whose potential curve was taken from Ref. 10 where it has been constructed from fluorescence spectral measurements and found to have a much deeper potential well than calculated in Ref. 9. For the dimer A and X states, Morse potentials were used which were specified with dissociation energies taken from Herzberg<sup>15</sup> and internuclear separations at the potential minima chosen to match the satellite peaks of the A-X transitions with those observed and reported in Ref. 10. An exception was again  $\text{Li}_2$ , its curves were taken from Ref. 4. The various rate constants used for the computations are tabulated for each alkali together with an appropriate source reference in Table II-1.

A computer program (see the appendix) was used to compute from Eqs. (II-1) through (II-22) the small-signal net gain versus wavelength from the A-X excimer and dimer transitions in all of the alkali-xenon systems (except francium) for input values of xenon concentration, gas temperature, and incident spectral pumping flux. Sample output results are shown in Figures II-2 and II-3. For these results a xenon concentration of  $3 \times 10^{20} \text{ cm}^{-3}$  and an incident flashlamp flux of  $1 \times 10^5 \text{ W/cm}^2\text{-}\mu\text{m}$  were chosen. Both of these values represent close to the maximum practical values achievable in the laboratory. The transverse propagation distance through the mixture of the pump radiation is assumed to be 1 cm.

TABLE II-1. Constants Specific to Each Alkali System Used in the Modeling Computations

Constant	Li	Na	K	Rb	Cs	Ref.
$A, \text{sec}^{-1}$	$3.67 \times 10^7$	$5.89 \times 10^7$	$3.69 \times 10^7$	$3.56 \times 10^7$	$2.50 \times 10^7$	16
$K_{AD_i}, \text{cm}^3$	$8.9 \times 10^{-23}$	$1.3 \times 10^{-23}$	$6.5 \times 10^{-23}$	$1.78 \times 10^{-23}$	$8.0 \times 10^{-23}$	2,17
$\Gamma_{\text{ass}D_i}, \text{cm}^{-3} \text{sec}^{-1}$	$\times \exp \frac{1.16}{T(\text{eV})}$	$\times \exp \frac{1.01}{T(\text{eV})}$	$\times \exp \frac{0.735}{T(\text{eV})}$	$\times \exp \frac{0.645}{T(\text{eV})}$	$\times \exp \frac{0.620}{T(\text{eV})}$	
	$8.0 \times 10^{-30} \times [\text{Xe}][\text{Li}]$	$8.0 \times 10^{-30} \times [\text{Xe}][\text{Na}]$	$8.0 \times 10^{-30} \times [\text{Xe}][\text{K}]$	$8.0 \times 10^{-30} \times [\text{Xe}][\text{Rb}]$	$8.0 \times 10^{-30} \times [\text{Xe}][\text{Cs}]$	2,18
$R_{X_{\text{Ex}}}$	2	2	2	2	2	19
$R_{X_{\text{Ex},f}}$	2	2	2	2	2	19
$R_{A_{\text{Ex}}}$	4	4	4	4	4	19
$R_{A_{\text{Ex},f}}$	6	6	6	6	6	19
$R_{X_{\text{Di}}}$	1	1	1	1	1	19
$R_{X_{\text{Di},f}}$	4	4	4	4	4	19
$R_{A_{\text{Di}}}$	1	1	1	1	1	19
$R_{A_{\text{Di},f}}$	12	12	12	12	12	19
$S_a (^{\circ}\text{K})$	$15.4 \times 10^4$	$10.33 \times 10^4$	$8.49 \times 10^4$	$7.6 \times 10^4$	$7.34 \times 10^4$	13
$S_b$	7.84	7.55	7.18	6.98	6.95	13

T2071



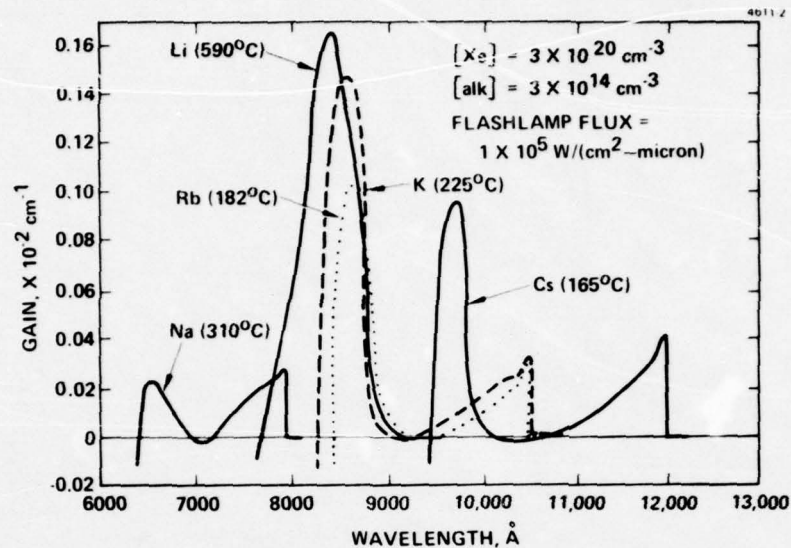


Figure II-2. Small-signal gain versus wavelength for the optically pumped alkali xenon excimer/dimer systems; lower alkali concentration results.

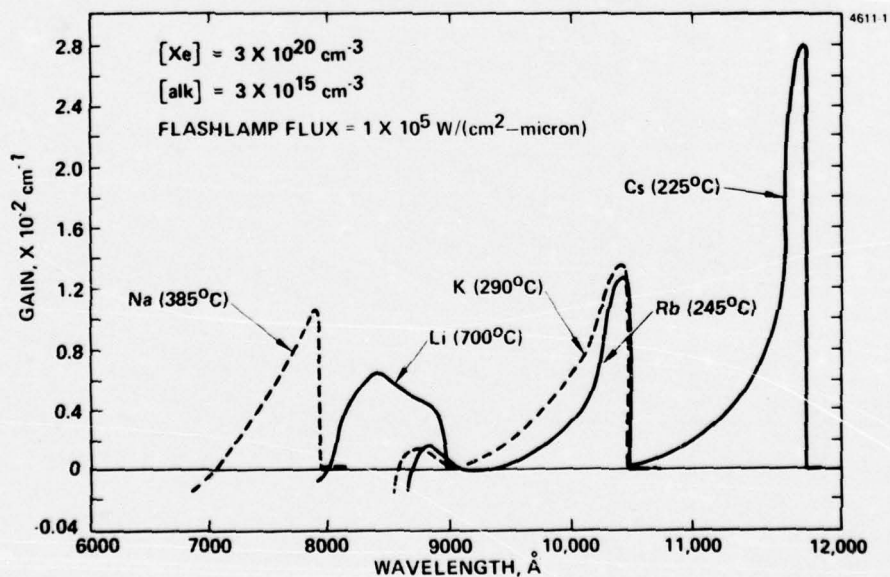


Figure II-3. Small-signal gain versus wavelength for the optically pumped alkali xenon excimer/dimer systems; higher alkali concentration results.

To obtain a useful comparison of the performance characteristics between the different alkalis, the results within each figure are plotted for equal concentrations of the alkali ( $[\text{alk}] \approx 3 \times 10^{14} \text{ cm}^{-3}$  in Figure II-2 and  $[\text{alk}] = 3 \times 10^{15} \text{ cm}^{-3}$  in Figure II-3).

The low alkali-concentration results in Figure II-2 show net gain present on both the excimer and dimer band for all of the alkalis. Except for lithium, the two bands are well separated with the dimer gain occurring at about a 1000 Å longer wavelength than the excimer gain. Due to the exceptionally deep excimer A-state potential well for Li, the excimer and dimer gain bands more closely overlap in this system and the ratio of excimer to dimer gain is greater for Li-Xe than for the other systems. The relatively low sodium-xenon excimer gain is due primarily to the higher temperatures required in conjunction with a relatively shallow A-state well depth.

The results for higher alkali concentrations plotted in Figure II-3 show the net gain on the excimer bands to be absent or reduced far below that of the dimer gain. This is due primarily to increased dimer absorption, which extends into the excimer band, and to the higher temperatures, which tend to reduce the inversion. The exception again is lithium, for which the excimer gain still dominates the gain bandwidth. The dimer satellite peak at 8900 Å is, however, beginning to reveal itself in the shape of the gain curve.

As the alkali density is increased further, the dimer gain will continue to increase and narrow onto the satellite peaks until an alkali concentration on the order of  $10^{17} \text{ cm}^{-3}$  is reached, at which point the gain at the satellite peak will start to decrease due to thermal degradation of the dimer inversion. Under the assumed values of xenon concentration and pumping flux, the satellite gains will at this point have reached quite high values (on the order of  $10^{-1} \text{ cm}^{-1}$ ).

The gain in both the dimer and excimer bands will increase as the xenon density is increased with, of course, a more rapid increase occurring on the excimer band. This is because the alkali resonance state, which feeds both the excimer and dimer A states, is being

pumped primarily on the excimer band for the range of temperature and xenon concentrations of interest here. This will continue up to a xenon concentration near  $10^{21} \text{ cm}^{-3}$ , where essentially all of the resonance-state population is in the form of excimers.

The gain will also increase with pumping flux up to levels on the order of  $10^6 \text{ W}/(\text{cm}^2 \mu\text{m})$ , where stimulated emission induced by the pump radiation will begin to cause a saturation of the pumping rate. Finally, the gains will, of course, decrease with the pump propagation distance into the mixture due to the reduced absorption coefficient for the pump radiation.

### 3. Conclusions

In conclusion, we have shown theoretically that practical laser gain coefficients should exist on the A-X excimer and dimer transitions of all of the alkali-xenon systems for flashlamp pumping under operating conditions which can be met in the laboratory. The theoretical model computes the wavelength profile of the net small-signal gain coefficient on the excimer and dimer bands of all of the alkali-xenon systems for input values of the xenon concentration, gas temperature (alkali concentration), and flashlamp flux.

The model is also clearly applicable for the lighter rare gases with the use of the appropriate alkali-rare-gas potential energy curves (e.g., from Ref. 9). The excimer gains are substantially reduced for the lighter rare gases due to the shallower A-state well depth but the dimer gains are, as expected, not seriously affected.

### B. Experimental Program

Experimental studies of flashlamp pumping of the K-Xe system were first carried out in the apparatus shown in Figure II-4. This apparatus was large enough to accommodate either the flashlamp-pumped tube or a transverse discharge used in the early phase of the



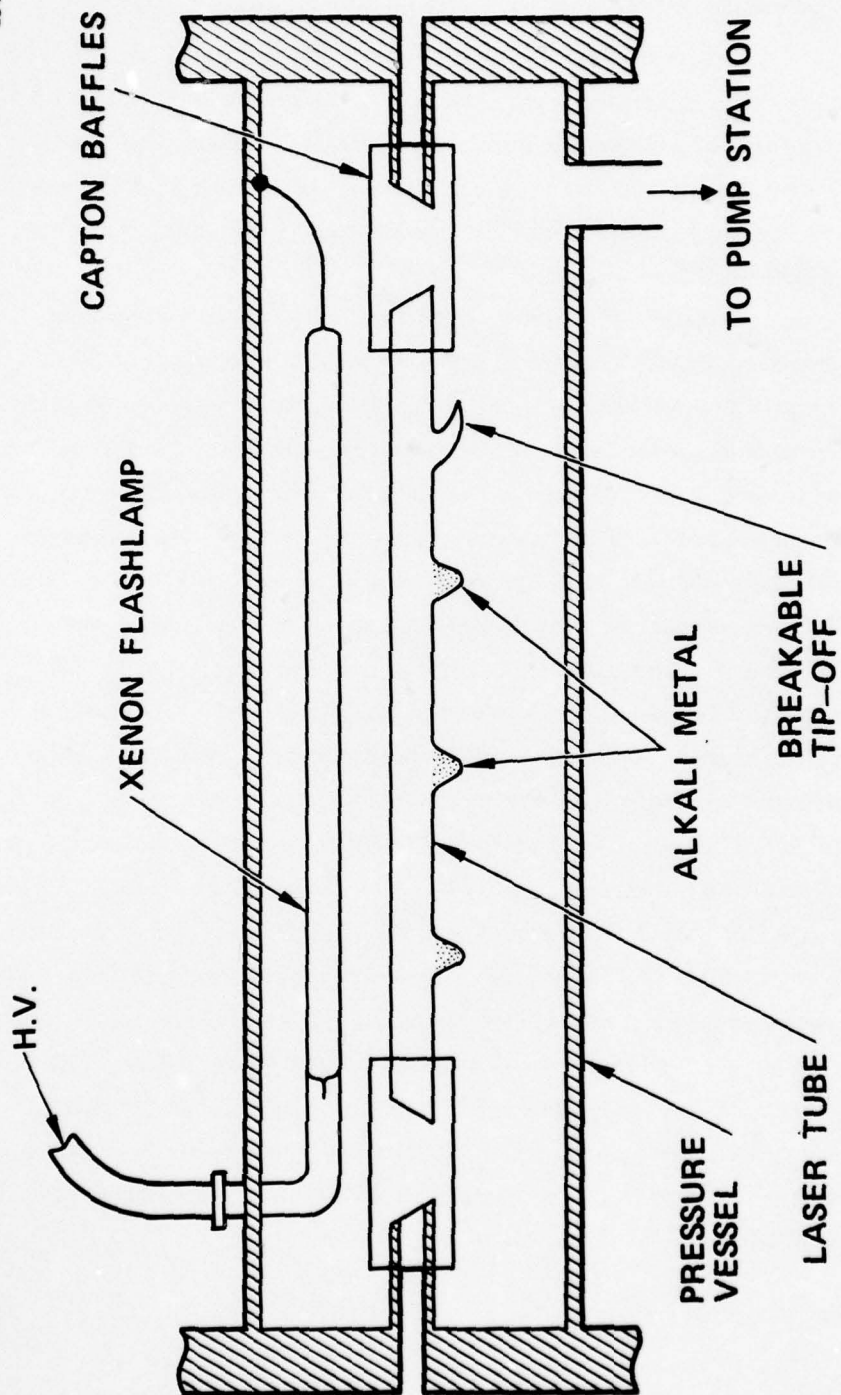


Figure II-4. Early experimental apparatus ~ flashlamp pumping.

program. The re-entrant Brewster windows allowed the vessel to be pressurized to several atmospheres. The vessel was wrapped with heating tape and could be brought to temperatures of up to 400°C.

Absorption coefficient measurements were initially made on the system to verify the quasi-static model used in the computer calculations. A comparison, showing good agreement between the measurements and the results of the theoretical model, is shown in Figures II-5 and II-6. Note the important contribution from the dimers, especially at the higher temperatures.

There were many difficulties with the initial flashlamp pumping experiments carried out in this pressure vessel. The main difficulty was with the high-voltage connection to the flashlamp which was within the heated region and, even more of a problem, was immersed in a xenon gas environment (which has a low breakdown threshold even at the high pressures used). The insulation provided for the connection would inevitably deteriorate at high temperature, and arcing would occur from the connection to the pressure vessel. The arcing would break both the tube and the flashlamp.

To remedy this problem and to upgrade and simplify the apparatus for flashlamp pumping, a new configuration was designed and fabricated which eliminated the need for the flashlamps within the pressure vessel. The new configuration is illustrated schematically in Figure II-7 and photographically in Figure II-8. This heavy-wall Pyrex laser tube operated reliably at total pressures of up to 20 atm and temperatures up to 350°C without serious physical deterioration. The quartz Brewster windows were fused onto quartz stems which in turn were fused with graded seals onto the re-entrant Pyrex tube. The tube was thus free of any adhesive which might degrade at the high temperatures used in the experiments. The arcing problem was eliminated, since the flashlamps were now in air and no longer in close proximity with the pressure vessel.

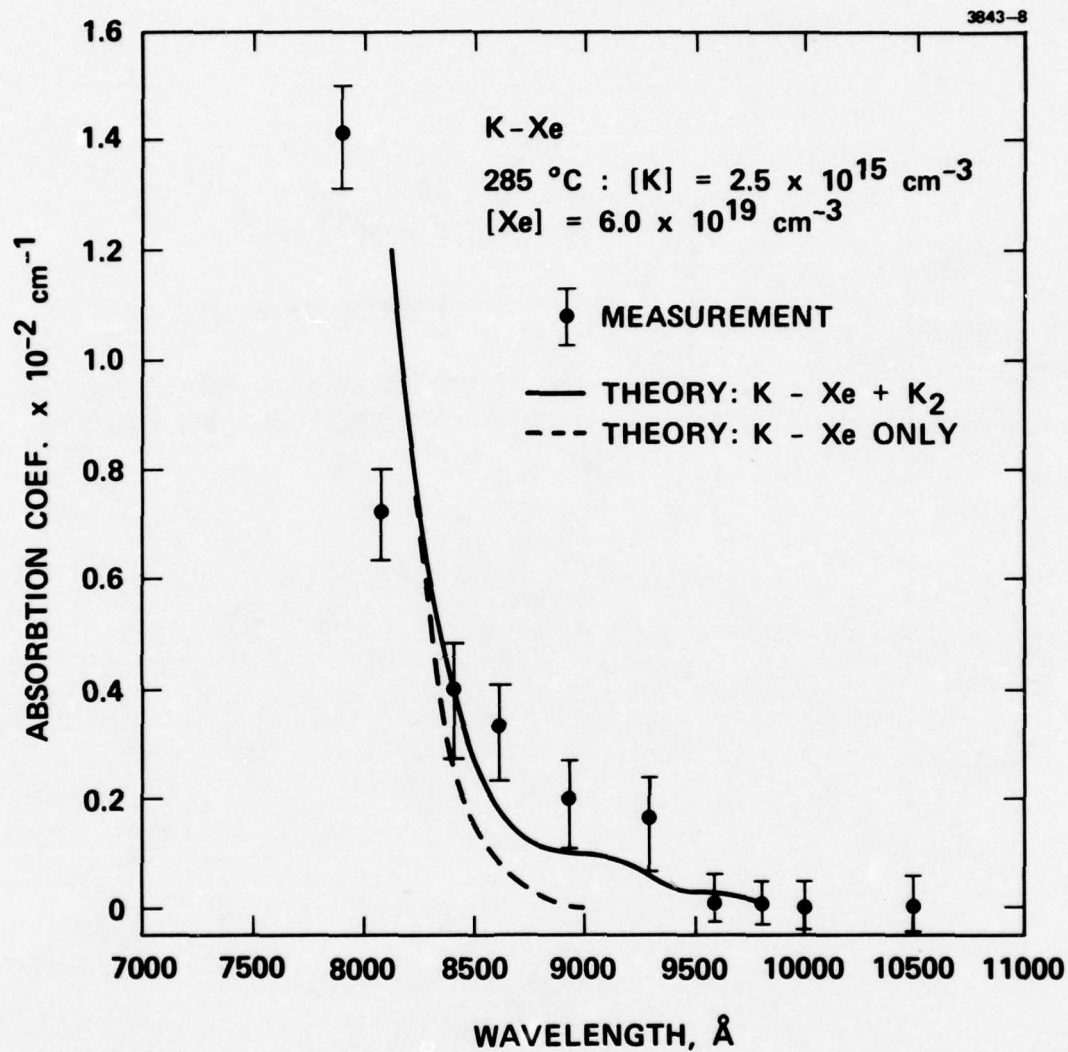


Figure II-5. Potassium-xenon absorption coefficient: comparison of measurements with theoretical model (low temperature results).



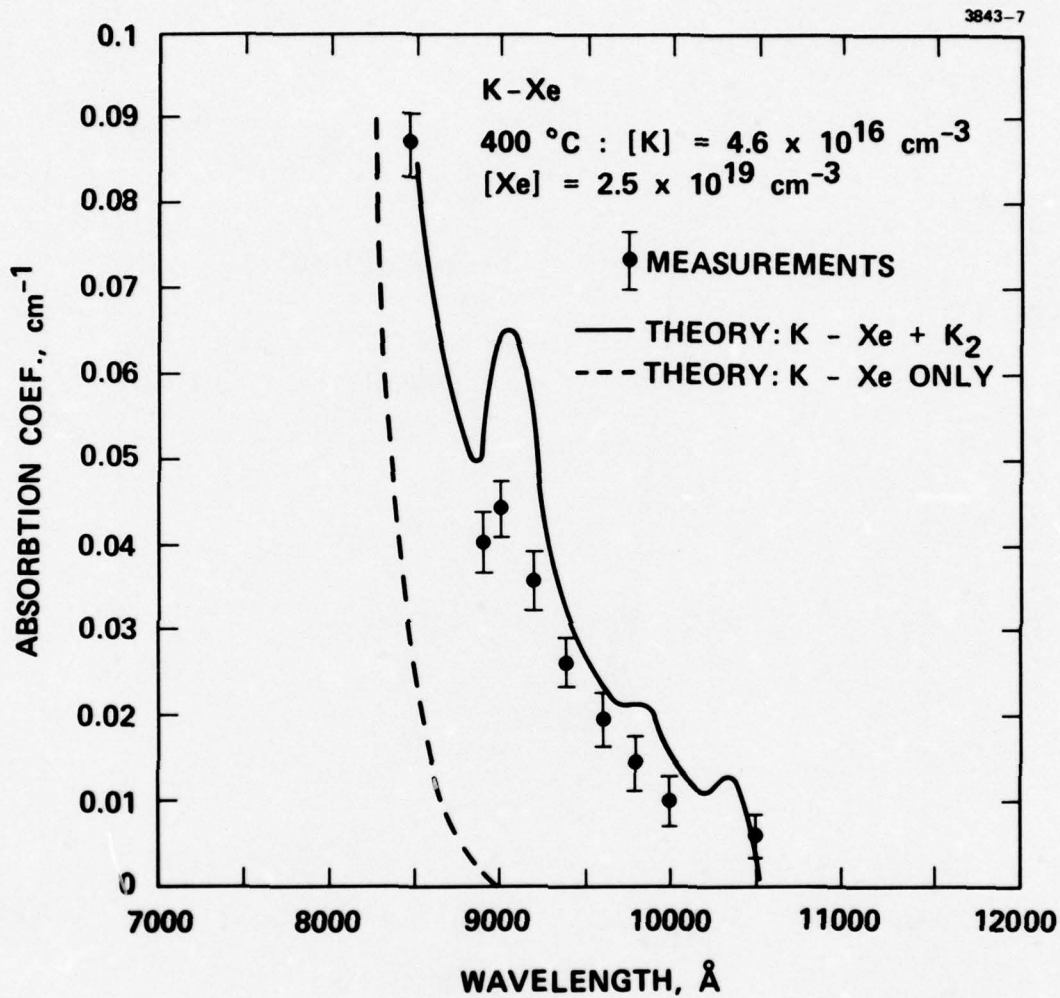


Figure II-6. Potassium-xenon absorption coefficient: comparison of measurements with theoretical model (high temperature results).

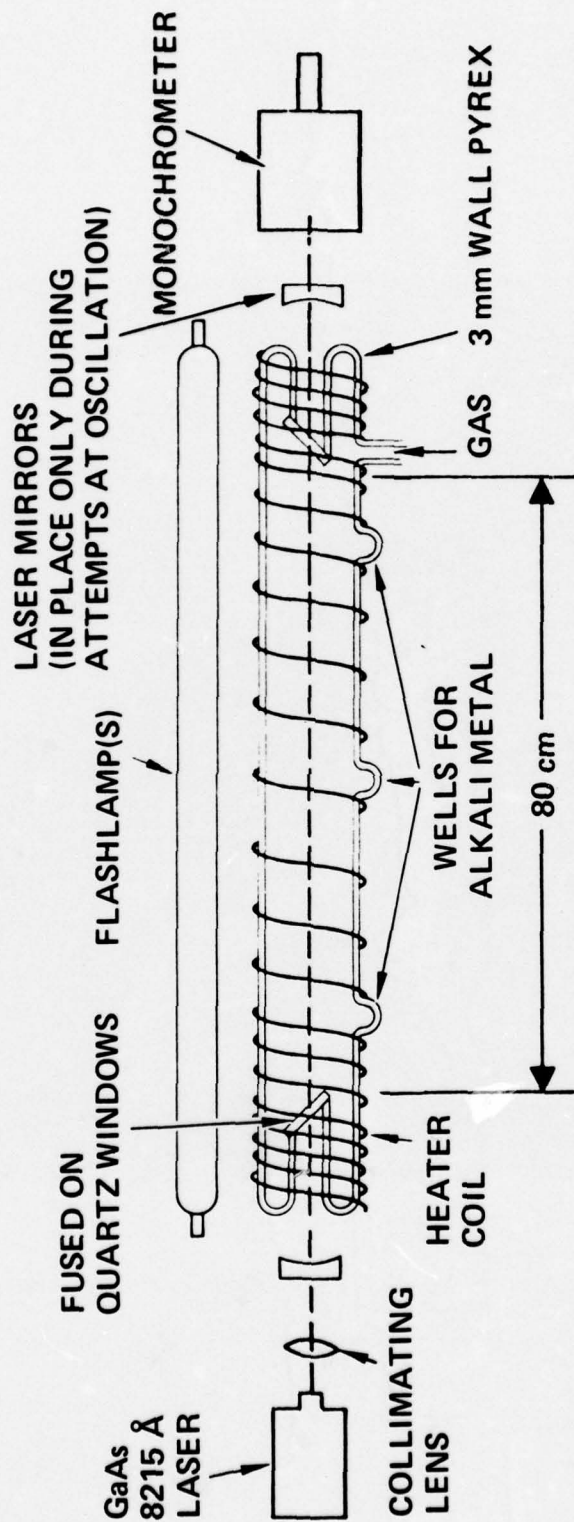


Figure II-7. Final optical pumping apparatus.

4141-4

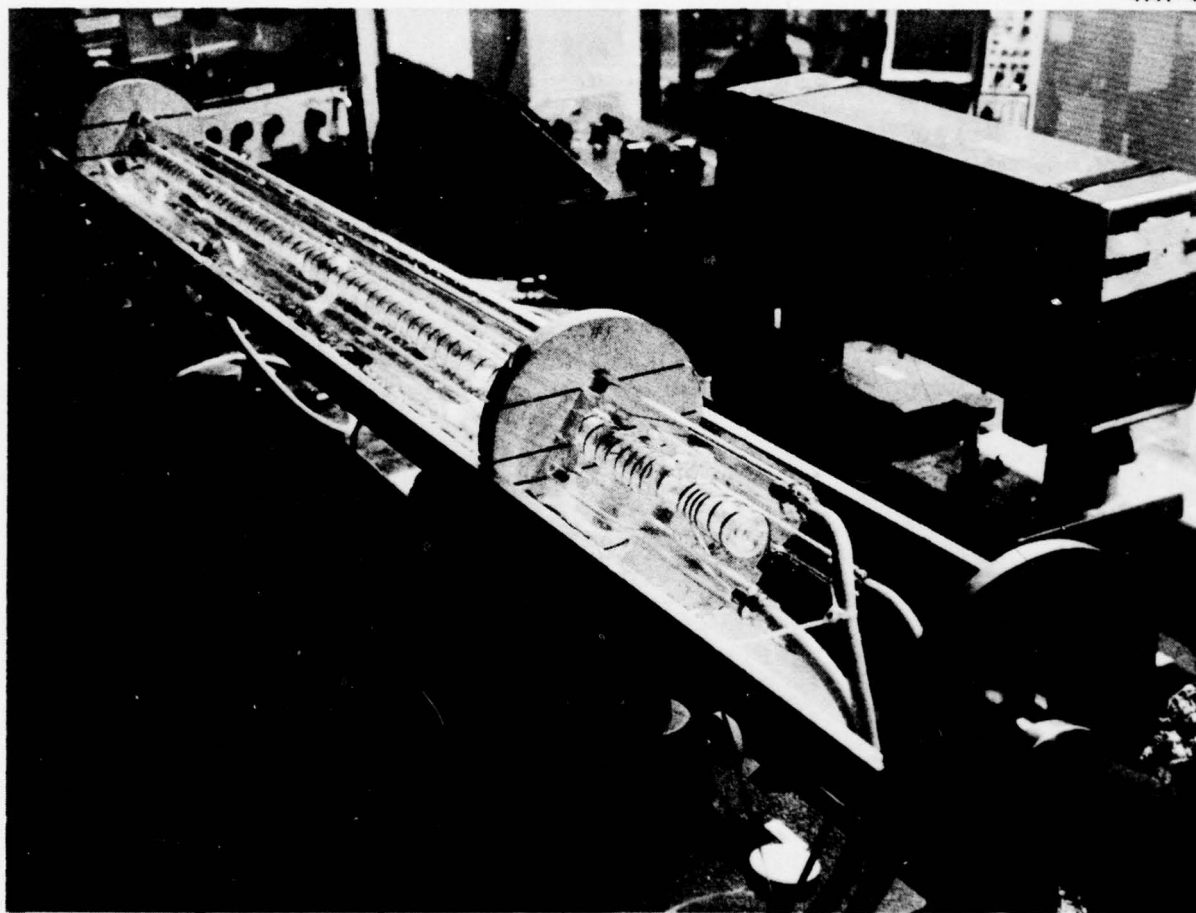


Figure II-8. Photograph of final optical pumping apparatus.



As indicated by Figure II-7, this apparatus was used both in attempts at achieving laser oscillation and for carrying out direct measurements of the laser gain with a GaAs probe laser. The excimer/dimer system studied was the K-Xe/K<sub>2</sub> system. Fluorescence measurements were not possible with flashlamp pumping in this setup, because the monochromator flooded with flashlamp radiation, which scattered down the axis of the laser tube.

The ability in the new configuration to view the longitudinal profile of the laser mixture made possible an important observation. As the tube walls were heated, a potassium aerosol cloud was observed to be evolved into the mixture. Within 1 to 2 hr after reaching a steady wall temperature, most of the aerosol cloud had dispersed, but some aerosol always remained (as evidenced by the forward scattering from a He-Ne laser beam passing through the mixture).

Measurements of the stimulated emission coefficient which can be carried out independent of the presence of cavity losses such as aerosols, window contamination, etc. were then undertaken. For this purpose a 100 nsec GaAs laser pulse was directed down the axis of the laser tube during the peak of the flashlamp pumping and again at a time outside the flashlamp pulse. The amplitudes of these two GaAs laser pulses as seen by the photomultiplier can then be used to calculate the net gain,  $\alpha_s(\lambda) - \beta_A(\lambda)$ , where  $\alpha_s(\lambda)$  and  $\beta_A(\lambda)$  are the stimulated emission and absorption coefficients, respectively. The GaAs laser used oscillates at 8220 Å. This wavelength lies outside the wavelength region for positive net gain, but this is immaterial for a measurement of  $\alpha_s(\lambda)$  as long as the probe laser is sufficiently transmitted by the laser medium to give a satisfactory signal-to-noise ratio at the photomultiplier.

A calibrated photodiode and a scanning multichannel spectrum analyzer were used to obtain absolute measurements of the flashlamp spectral output power (see Figure II-9). These measurements indicated that the flashlamp flux at the axis of the laser tube is within a factor of two of the flux value assumed in the modeling result shown in Figure II-10.

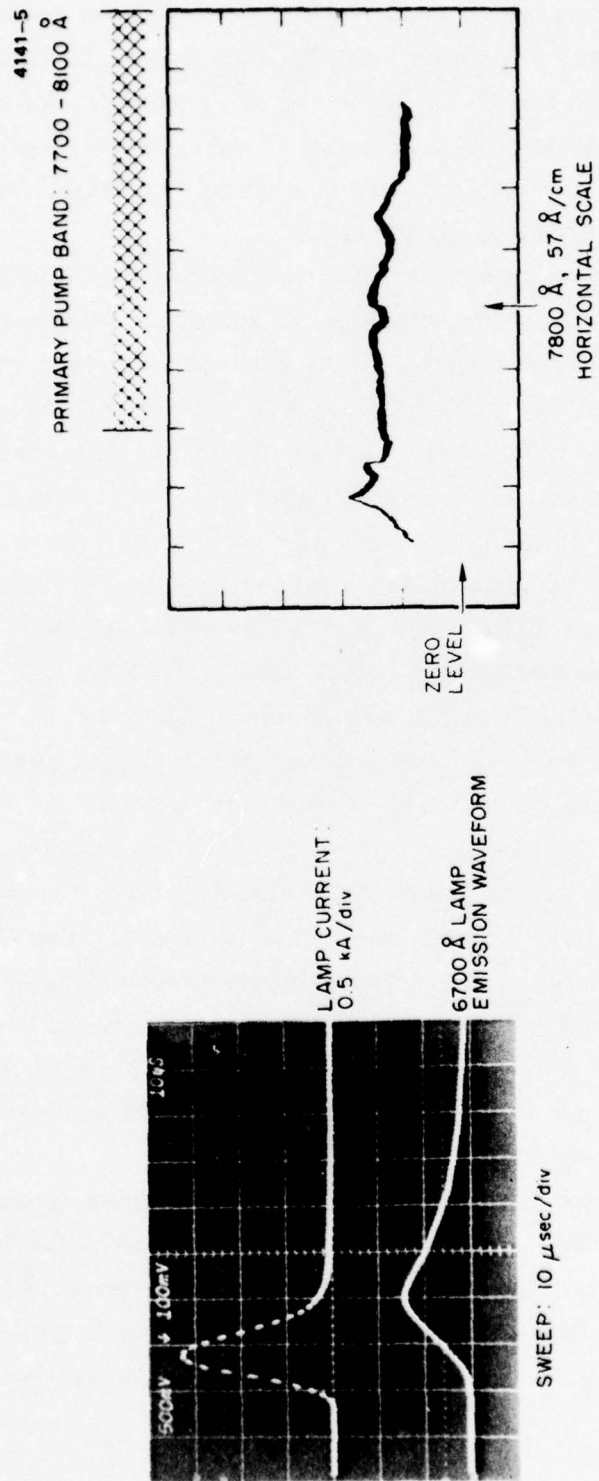


Figure II-9. Flashlamp output measurements.

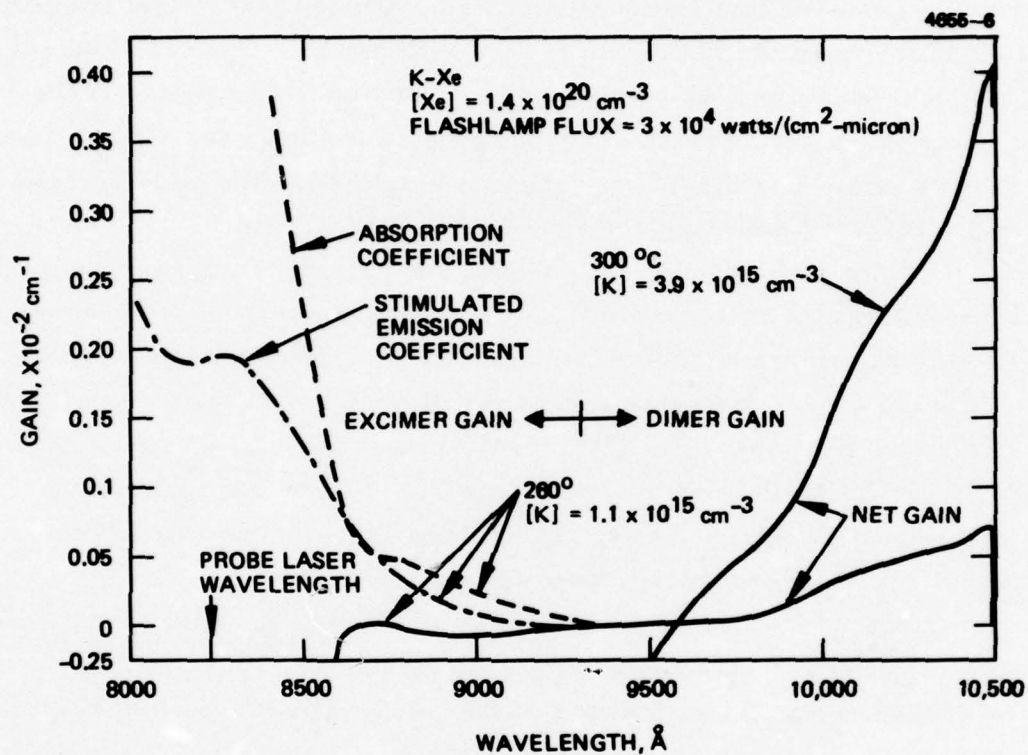


Figure II-10. Theoretical small signal gain coefficient versus wavelength for K-Xe for attained experimental conditions.



Results of a typical gain measurement are shown in Figure II-11. Shot-to-shot fluctuation on the probe laser throughput due to thermal refractive disturbances of the medium were reduced to about the 20% level, as can be seen in the scatter of the probe laser reference pulse height shown on the right side of the oscillogram. The probe laser amplified pulse heights exhibit a 50% amplification as shown by the 3 shots taken during flash-lamp pumping on the left hand side of the oscillogram. For the 80 cm gain path employed, this value corresponds to a stimulated emission coefficient of  $0.5 \times 10^{-2} \text{ cm}^{-1}$ .

This does not indicate positive net gain; it is a direct measure of the effectiveness of our optical pumping arrangement for producing KXe excimers and of their stimulated emission rate at a particular wavelength. For the given experimental conditions, the value of the stimulated emission coefficient is within a factor of 2 of the value predicted by the model, as shown in Figure II-1. This experimental information is extremely useful for comparison to our theoretical model and its subsequent refinement and development.

A gain measurement at  $6328 \text{ \AA}$  on the B-X  $\text{K}_2$  dimer band was also obtained during a check on beam steering effects caused by refractive disturbances induced in the medium by the flashlamp discharge. The results of this measurement are shown in Figure II-12. The lower trace shows the time profile of the flashlamp emission, and the upper trace shows the time profile of the amplitude of the He-Ne beam after passing through the mixture and into a monochromator. The irregular variations on the He-Ne signal are, as anticipated, from the beam slewing across the monochromator slits as a result of induced refractive disturbances. The time delay to the first irregularity is an acoustic transit time between the flashlamp and the laser tube and, in fact, varies as the square root of the temperature, as it should for an acoustic disturbance.

The initial rise of the He-Ne signal, which begins with the flashlamp emission, could not have been caused by acoustic disturbance and is, in fact, gain,  $\alpha_s(\lambda) - \beta_A(\lambda)$ , as discussed above. It is caused by

4423-4

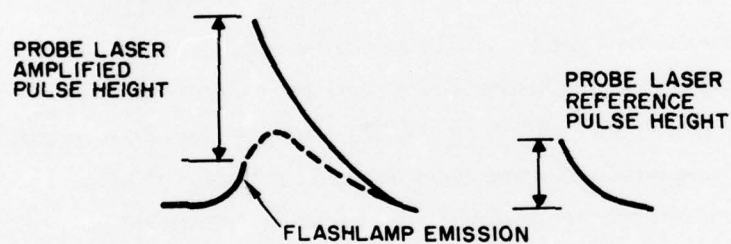
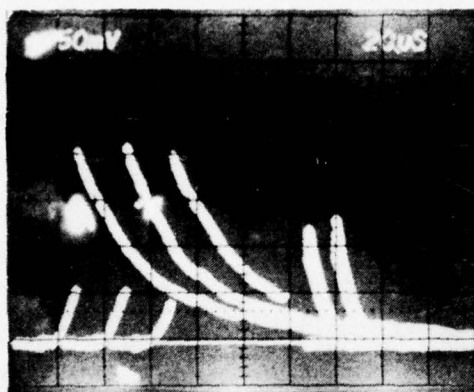
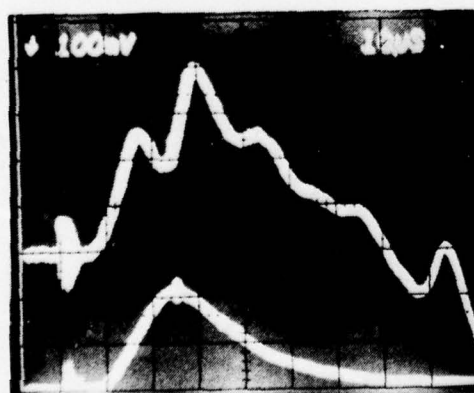


Figure II-11.  
Gain measurement:  
8220 Å.

TUBE TEMPERATURE = 260 °C  
 $[K] = 8 \times 10^{14} \text{ cm}^{-3}$   
 $[Xe] = 1.4 \times 10^{20} \text{ cm}^{-3}$

4423-3



He-Ne  
LASER  
(DC LEVEL  
= 8 cm)

FLASHLAMP  
EMISSION

Figure II-12.  
Gain measurement:  
6329 Å.

TUBE TEMPERATURE = 275 °C  
 $[K] = 2 \times 10^{15} \text{ cm}^{-3}$   
 $[K_2] = 1 \times 10^{13} \text{ cm}^{-3}$   
 $[Xe] = 1.4 \times 10^{20} \text{ cm}^{-3}$

stimulated emission on the B-X transition of  $K_2$ . Unfortunately, the entire B-X band is blue-shifted from the parent resonance line so that a population inversion on this transition can never be obtained under two-temperature equilibrium conditions. The transition, therefore, has no potential for excimer laser action, which is why it was not included in the modeling calculations. The measurements shown in Figure II-12 are instructive, however, especially in pointing out the necessity for taking gain measurements before the arrival of the acoustic disturbances which can cause slewing of the probe beam. The gain measurements at 8220 Å described above were carried out within this time frame.

Attempts to achieve laser oscillation in the apparatus of Figure II-7 were carried out on both the K-Xe excimer band and the  $K_2$  dimer band using mirrors with 99.0 to 99.9% reflectivity throughout each band. Oscillation was not observed on either band. Failure to achieve oscillation on the excimer band can be understood on the basis of the modeling prediction of negative net gain on the excimer band under the conditions of the experiment (Figure II-10). Practical positive net gain is predicted for a factor of three increase in both the Xe concentration and flashlamp flux, which can probably be accomplished with an upgraded laboratory setup. The failure to achieve oscillation in the dimer band is felt to be due primarily to optical losses at the Brewster angle windows and to inadequate alignment of the laser mirrors. Mirror alignment is more difficult for the dimer than the excimer band because, at the temperatures required for a high dimer gain, the mixture is opaque to the He-Ne alignment laser.



### III. DISCHARGE PUMPING OF THE ALKALI EXCIMER AND DIMER MOLECULES

The broadband optical pumping technique described in the previous section was chosen as the most expedient means to demonstrate gain. It is also dimensionally scalable to a transverse dimension of ~10 cm. However, efficiency limitations eliminate this pumping technique as a candidate for practical device development. Discharge pumping is the most promising technique for achieving efficient and scalable high average power device development; this section presents the results of theoretical and experimental studies on discharge pumping of the potassium-argon excimer/dimer system.

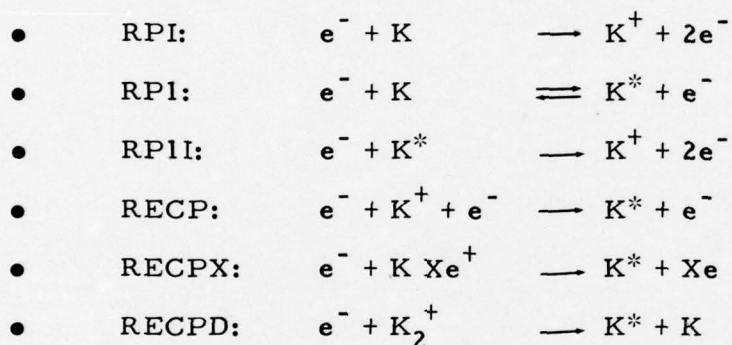
#### A. Theoretical Program

The optical pumping system was a steady-state model. Steady-state modeling is justifiable for optical pumping since the relaxation times of all optical pumping and kinetics processes are short compared to flashlamp pulse duration. On the other hand, this is generally not the case for discharge pumping. In particular, such discharges tend to be unstable and it is not clear a priori that a steady-state discharge mode can ever be reached. A full time-dependent discharge model is presented below.

The discharge model follows the time evolution in the discharge of the concentration of six excited and ionized alkali states, the electron and gas temperatures, and the net small-signal gain coefficient at two wavelengths, one near the peak of the excimer gain band and the other at the dimer satellite wavelength. The time dependence of the circuit current and voltages is included, as are a series resistance, series inductance, and storage capacitor as the modeled circuit elements.

The plasma and gas kinetic processes included in the rate equations governing the species concentrations are listed below. The rate constants, cross sections, and equilibrium constants for these processes can be found in the computer code listing included in the appendix, and, together with a source reference, in Table III-1. An R label refers to a plasma process and a G label refers to a gas kinetic process. In the listing, a B at the end of the label refers to the back reaction, which is computed by detailed balancing using the appropriate equilibrium constant or Boltzmann factor reaction. The particular case presented refers to a potassium-xenon mixture.

The plasma processes modeled are:



The gas kinetic processes modeled are:

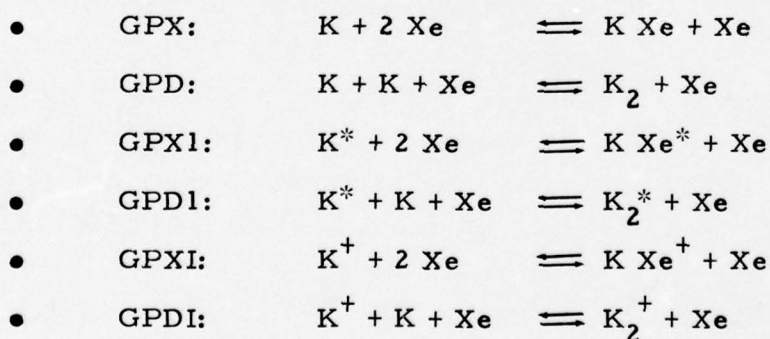


TABLE III-1. List of Cross Sections, Rate Constants, Equilibrium Constants, and Source References Used for Discharge Pumped K-Xe/K<sub>2</sub> Modeling

Parameter	Value	Reference
Inelastic electron collision cross sections: initial slope of cross sections w.r.t. energy above threshold		
CPI	$6 \times 10^{-15} \text{ cm}^2/\text{eV}$	20
CPI	$0.5 \times 10^{-16} \text{ cm}^2/\text{eV}$	20
CPII	$5 \times 10^{-16} \text{ cm}^2/\text{eV}$	Rough estimate
Recombination coefficients:		
Three-body RECP	$2.28 \times 10^{-26} \times [\text{K}^+] \times [\text{Ne}]^2 \times \text{Te}^{(-4.39)} \text{ cm}^{-3} \text{ sec}^{-1}$	22 (Cesium)
Dissociative - ( $\text{K Xe}^+$ )		Rough estimate
RECPX	$3.3 \times 10^{-5} \times [\text{K}] \times [\text{Xe}^+] \times [\text{Ne}] \times \text{Te}^{(-0.67)} \text{ cm}^{-3} \text{ sec}^{-1}$	
Dissociative - ( $\text{K}_2^+$ )		
RECPD	$3.3 \times 10^{-5} \times [\text{K}_2^+] \times [\text{Ne}] \times \text{Te}^{(-0.67)} \text{ cm}^{-3} \text{ sec}^{-1}$	Rough estimate
Photoionization cross section:		
CPII	$0.5 \times 10^{-19} \text{ cm}^2$	22
Electron elastic cross section:		
CEL	$5.5 \times 10^{-16} \text{ cm}^2$	20
Heavy particle elastic cross section:		
CDIF	$1 \times 10^{-15} \text{ cm}^2$	Rough estimate
Gas kinetic rates:		
GPD	$8 \times 10^{-32} \times [\text{Xe}] \times [\text{K}] \times [\text{K}^+] \text{ cm}^{-3} \text{ sec}^{-1}$	2
Equilibrium constants:		
KAEX	$2.2 \times 10^{-23} \times \exp(0.074/\text{Tg}) \text{ cm}^3$	24 (Rubidium)
KXDI	$1.8 \times 10^{-22} \times \exp(0.56/\text{Tg}) \text{ cm}^3$	2
KADI	$6.5 \times 10^{-23} \times \exp(0.735/\text{Tg}) \text{ cm}^3$	2
Optical rates	All radiative rates, absorptive and stimulated emission cross sections, and their dependences on temperature and density are taken from Section IIA.	

T1926



The radiative processes modeled are:

- AT:  $K^*$   $\longrightarrow$   $K + h\nu$  (TRAPPED)
- AP:  $K^{**}$   $\longrightarrow$   $K + h\nu$
- AP:  $KXe^*$   $\longrightarrow$   $KXe + h\nu$
- AP:  $K_2^*$   $\longrightarrow$   $K_2 + h\nu$

Under the conditions we consider ( $[Xe] \approx 1 \times 10^{20} \text{ cm}^{-3}$ ), the gas kinetic rates dominate the electron collisional rates in controlling the population of the molecular states. At the gas temperature to be maintained, we therefore assume thermal equilibrium between the molecular states and their dissociation products. As in the optical pumping model, an exception is the A state of  $K_2$ , for which radiative losses are included since they can compete with the dissociation rate.

The average electron energy was computed by solving the electron energy equation:

$$J \cdot E_{\text{disch}} = \sum_i (\text{INELASTIC COLLISION RATE } (Te))_i \times E_i$$

$$+ (\text{ELASTIC COLLISION RATE}) \times 2 \left( \frac{M_e}{M_m} \right) \times Te$$

(III-1)

where  $J$  is the current density,  $E_{\text{disch}}$  is the discharge electric field,  $E_i$  is the inelastic energy loss for the  $i^{\text{th}}$  process, and  $M_m$  and  $M_e$  are the masses of the  $M$  species and electron, respectively. Resonance level pumping was assumed to dominate the inelastic process contributing to the energy equation. For this reason and the fact that the molecular association rates which pump the upper laser levels dominate the loss of the resonance level population, the predicted efficiency for converting discharge power to laser power is essentially

the quantum efficiency of the transition which is lasing. A Maxwellian energy distribution was assumed, which should be a fair approximation since the two-step alkali ionization processes dominate the single-step alkali ionization under the operating conditions considered. Only the latter process requires electrons with energies in the tail of the distribution, where a large reduction of the number of electrons from a Maxwellian distribution is known to occur. Excitation and ionization of the rare gas is neglected entirely for this reason.

The electron collisional rate constants are expressed in a form which results from assuming a linear rise of the cross section with energy above threshold:<sup>25</sup>

$$R(T_e) = \frac{6 \cdot 10^2}{(e/m_e)/\pi} \left. \frac{d\sigma}{d\epsilon} \right|_{\epsilon_0} \left( \frac{2}{m_e} T_e \right)^{3/2} \exp(-\epsilon_0/T_e) \left( 1 + \frac{\epsilon_0}{2T_e} \right), \quad (\text{III-2})$$

where  $\epsilon_0$  is the threshold energy for the excitation of ionization process,  $d\sigma/d\epsilon|_{\epsilon_0}$  is the rate of the cross-section rise with energy above threshold, and  $m_e$  and  $e$  are, respectively, the electron mass and charge.

Also, in solving Eq. (III-1) we use an expression for the drift velocity obtained from Ref. 25:

$$V_{\text{drift}} = (2 T_e / M_{\text{Xe}})^{1/2}, \quad (\text{III-3})$$

where  $M_{\text{Xe}}$  is the mass of the xenon atoms.

The gas temperature is calculated by assuming that all of the discharge power goes into gas heating and that heat is removed only by thermal conduction to a wall (assumed cylindrical):

$$\frac{dT_G}{dt} = J \bullet E_{\text{disch}} / (3/2 [M]) - (\text{THERMAL CONDUCTIVITY})$$

$$\times \left( \frac{4.8}{\text{DIAMETER}} \right)^2 \times (T_G - T_{\text{WALL}}) \quad (\text{III-4})$$

The discharge circuit response is governed by the familiar circuit equations:

$$V_{\text{disch}} = V_c(t) - L \times \frac{dI}{dt} - R \times I \quad (\text{III-5})$$

$$V_c(t) = V_{\text{charge}} - 1/C \int I dt, \quad (\text{III-6})$$

where  $V_{\text{disch}}$  is the discharge voltage,  $V_c$  is the capacitor voltage,  $V_{\text{charge}}$  is the initial charging voltage,  $I$  is the discharge current, and  $R$ ,  $L$ , and  $C$  are the series resistance, inductance, and storage capacitance, respectively.

The optical gain of the system is calculated from the relationship,

$$\text{GAIN}(\lambda) = \sigma_{\text{STIM, ex}}(\lambda) \left\{ [KXe^*] \times \frac{\exp(-V_{A, \text{Ex}}(\lambda)/T_G)}{(K_{\text{eq A, Ex}} \times 3/2)} \right.$$

$$\left. - 2 \times [K] \times [Xe] \times \exp(-V_{x, \text{Ex}}(\lambda)/T_G) \right\}$$

$$+ \sigma_{\text{STIM, Di}}(\lambda) \left\{ [K_2^*] \times \frac{\exp(-V_{A, \text{Di}}(\lambda)/T_G)}{(K_{\text{eq A, Di}} \times 1/2)} \right.$$

$$\left. - 0.25 \times [K]^2 \times \exp(-V_{x, \text{Di}}(\lambda)/T_G) \right\} \quad (\text{III-7})$$



$$\sigma_{\text{STIM}}^{(\lambda)} \left| \begin{smallmatrix} \text{Ex} \\ \text{Di} \end{smallmatrix} \right| = (A_E/2c) \times \lambda^2 \times R_{\text{Ex}}^2 \times \left. \frac{dR(\lambda)}{d\nu} \right| \left| \begin{smallmatrix} \text{Ex} \\ \text{Di} \end{smallmatrix} \right|, \quad (\text{III-8})$$

where the notation follows that used in Section II. A.

As shown by the computer code listing in the appendix, the coupled rate equations governing all of the above processes are integrated numerically using a time step chosen by the user and altered, if desired, during the course of the computer run. The computer program is written for the PDP10 computer.

#### B. Results and Discussions

The results of three computer runs of the above model are presented in Figures III-1 through III-3. The series inductance,  $L$ , and resistance,  $R$ , are assumed equal to zero in these runs.

The results presented in Figure III-1 are for an avalanche discharge through a 10 atm potassium-xenon mixture at two different temperatures. As in the optical pumping case, the lower temperature result shows most of the gain occurring on the excimer band (8500 Å), and the higher temperature case shows the highest gain occurring on the dimer band. In both cases the model predicts that a fairly high  $E/N$  value of  $\sim 10^{-11}$  V/(cm · [K] cm<sup>-3</sup>) is required to give practical gain coefficients of  $\sim 1\%/cm$ .

The results in Figure III-1 are for an infinite storage capacitance, and illustrate an important feature of the discharge kinetics. Unlike the other popular class of discharge pumped excimer systems, the rare gas monohalides, the alkali-rare-gas discharge appears in the modeling to be stable against ionization instabilities. This is due to two causes: first, to the fact that the discharge is recombination stabilized rather than attachment stabilized; and second, to the fact that the ground-state potassium population is depleted during the discharge, which saturates the ionization.

$$[\text{Xe}] = 1 \times 10^{20} \text{ cm}^{-3}$$

$$C = \infty$$

$$\Phi_{u.v.} \approx 0$$

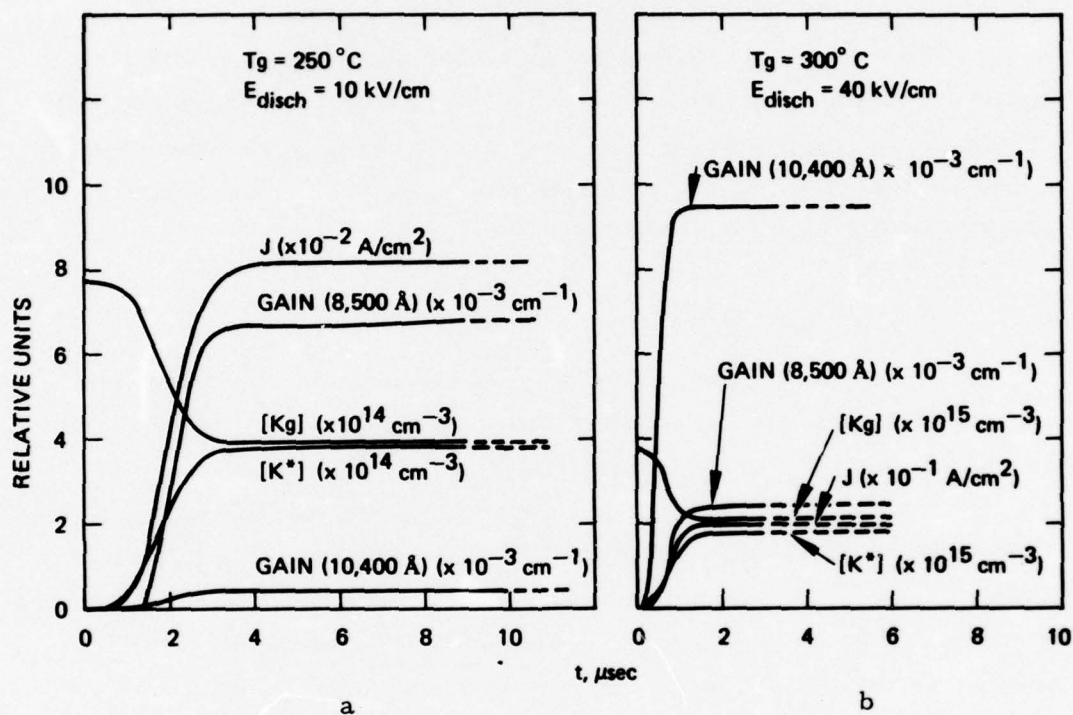


Figure III-1. Theoretical modeling results for avalanche sustained discharge pumping of the K-Xe/ $\text{K}_2$  system. (a) Low temperature results. (b) High temperature results.

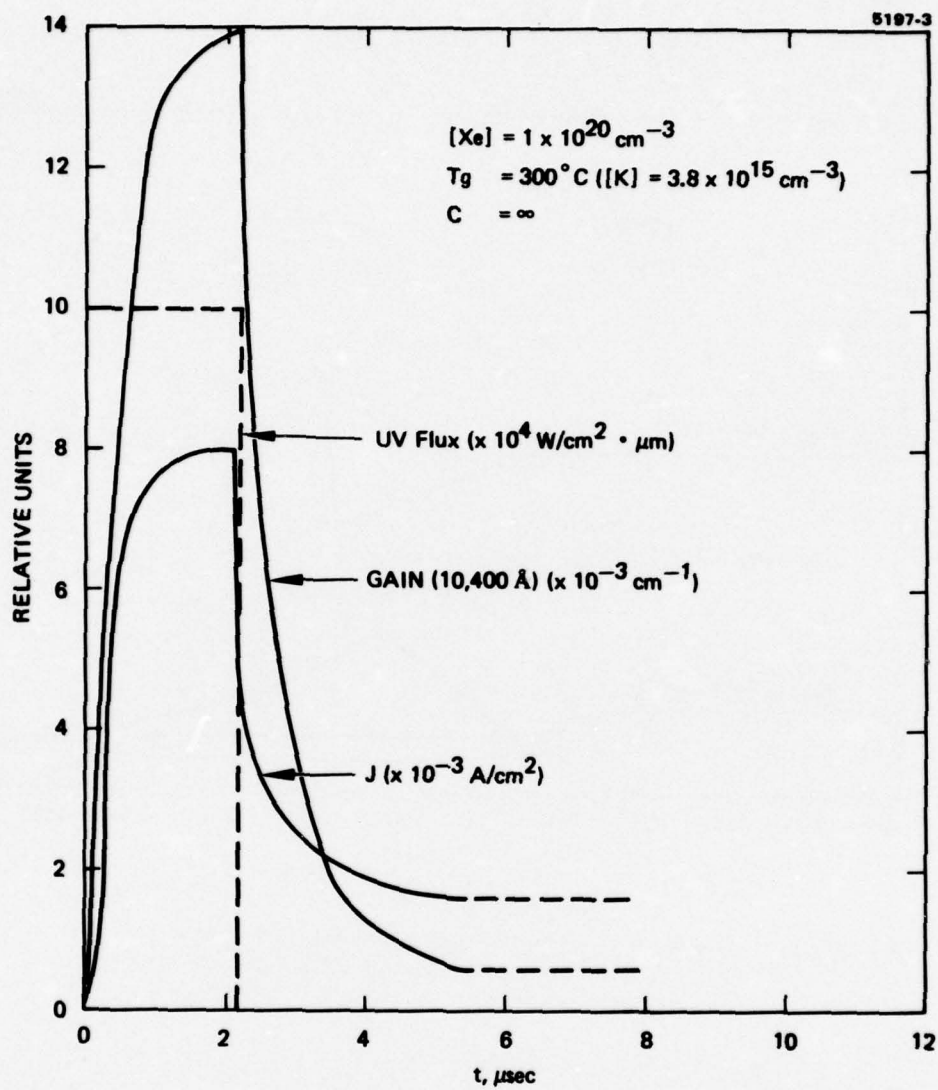


Figure III-2. Theoretical modeling results for uv sustained discharge pumping of the K-Xe/K<sub>2</sub> system.



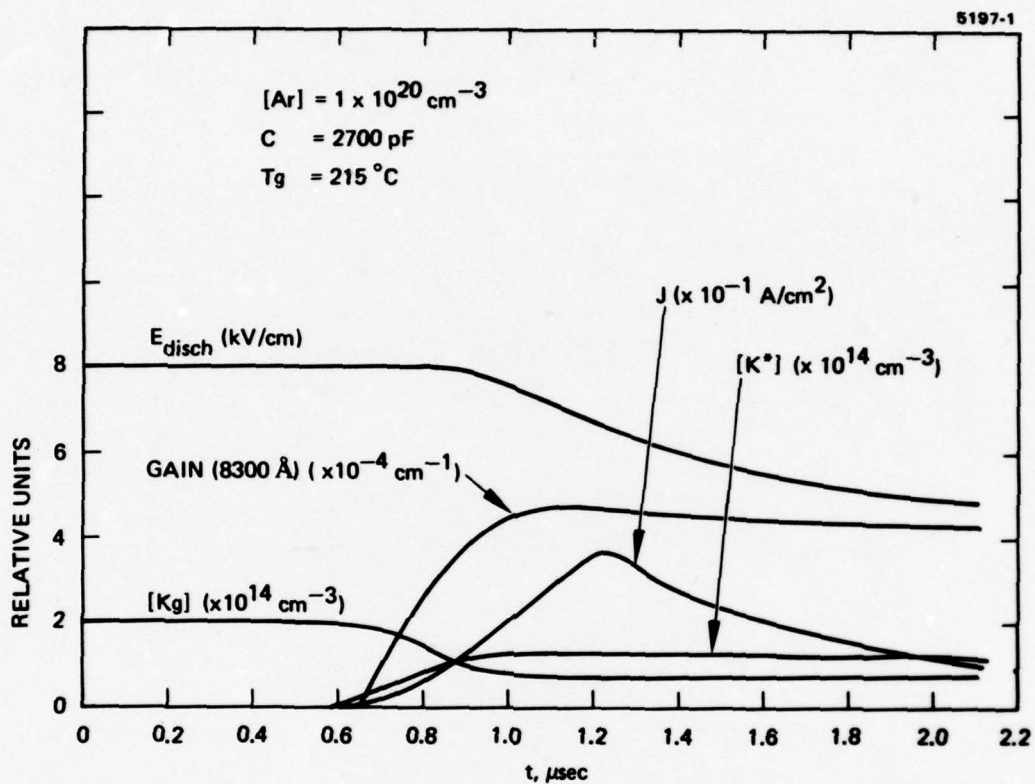


Figure III-3. Theoretical modeling results for avalanche sustained discharge pumping of K-Ar system under conditions achieved in early discharge experiments.

Results for a uv-sustained K-Xe discharge are presented in Figure III-2. Here a comparable dimer gain coefficient is achieved at half the discharge  $E/N$  value required for the 300°C avalanche discharge case. Very high flashlamp brightness is required here and results in an extremely low overall efficiency. Since the higher efficiency avalanche discharge is predicted to be stable, there is no apparent advantage in operating the discharge in this mode.

Finally, in Figure III-3 we present modeling results for a K-Ar discharge with a finite storage capacitance at conditions near those achieved in the early discharge experiments. The potassium density is seen to be too low to yield a practical gain coefficient in this case. The results from the model show approximately an order of magnitude lower peak current density than was measured in the experiment at this voltage and capacitance. We attribute this to too high a value estimated for the dissociative recombination rates used in the model.

### C. Experimental Program

The primary emphasis of the experimental part of this program was directed toward achieving a diffuse discharge in potassium-argon mixtures at high pressure. Discharge dimensions and configuration were chosen to obtain experimental results which are directly applicable to scaling considerations for high-power laser applications. Thus, the discharge apparatus was designed around a transverse electrode arrangement with the width-to-gap ratio equal to two and the length-to-gap ratio equal to ten.

In addition to the design and fabrication of the electrode apparatus, considerable attention was devoted to solving the "aerosol" problem encountered in our previous work. Experiments conducted in a carefully controlled environment under a variety of experimental conditions have demonstrated that "aerosol-free" mixtures of potassium and argon can be obtained at elevated temperatures and pressures provided temperature gradients are minimized and the potassium vapor is evolved at low pressure. Some of our experiments indicate that the former requirement is more important than the latter.

During the latter part of this study, we achieved a diffuse discharge in a potassium-argon mixture at high pressure (7 atm). The details of these experiments will be discussed in the following section, but it is noteworthy that this discharge has very good spatial homogeneity, exhibits strong K-Ar excimer emission, and that no form of auxiliary preionization was required. Potassium atom densities used to date are high enough to provide significant optical gain; equilibrium potassium vapor densities at temperatures up to 350°C have been achieved.

#### 1. Discharge Apparatus

A major concern in the apparatus design was electrode size and configuration. An electrode size of 2 x 13.5 cm with a gap spacing of 1 cm was chosen initially because it is small enough to be convenient but also large enough to give meaningful results in terms of scaling the system for high-power laser applications. To allow maximum flexibility in choice of discharge mode for optimum laser operation, we included provisions in the apparatus for a high-intensity flashlamp. This provides the option of discharge operation in a uv preionized mode, a uv-sustained mode, or simply as an over-voltaged avalanche discharge without preconditioning. A diagram of the first version of this system is shown in Figure III-4. A pyrex pressure vessel was selected to provide maximum viewing capability of the discharge. This design proved to be too difficult to fabricate, however, so an alternate apparatus using a stainless-steel pressure vessel with a pyrex liner for electrical isolation was designed and assembled. This apparatus is illustrated in Figure III-5, which shows the electrodes, re-entrant Brewster angle windows, and a large side window for viewing the discharge along its entire length. This apparatus met the high pressure (10 atm) and discharge viewing requirements, but problems developed with the O-ring seals after several temperature cycles between 25 and 350°C. Chemical reactions among several components caused difficulties, and thermal gradients contributed to aerosol formation.



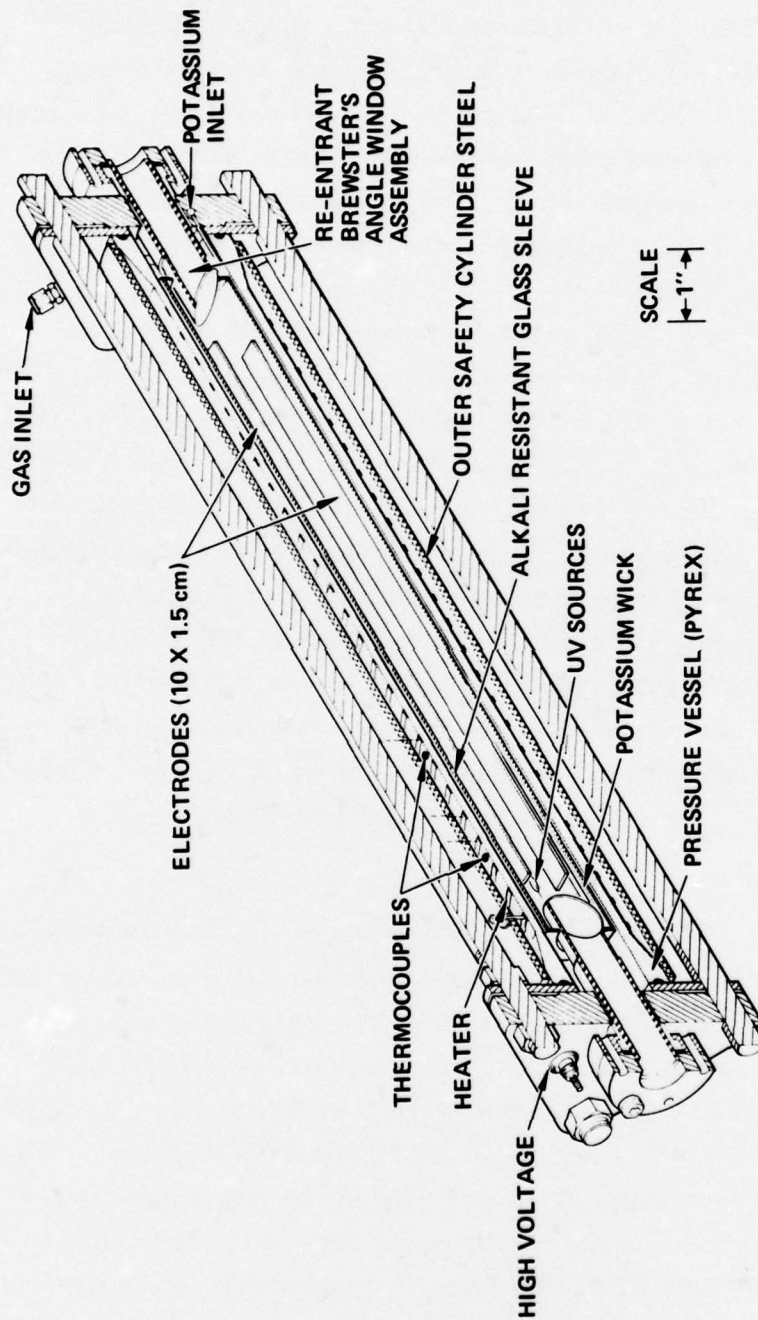


Figure III-4. Alkali-rare-gas discharge tube, design 1.

We revised that system by using metal vacuum flanges and eliminating the pyrex liner. A photograph of this apparatus is shown in Figure III-6. These modifications virtually eliminated chemical corrosion problems and aerosol formation. Discharge viewing length was compromised because of the limited maximum window size available with a metal seal; however, additional windows could be added for better discharge viewing if required. It is with the revised device that we observed spatially uniform discharges in a potassium-argon mixture at 7 atm and 300°C.

The electrode profile which we have used to date is planar, with the sides and ends contoured to the curvature of an ellipse. The electrode is flat over a region ~1.3 times the discharge gap and then joins smoothly to an ellipse. In previous work,<sup>26</sup> we found the electric field between electrodes of this type to be uniform to better than 1%, as determined by electrostatic potential plots using resistance paper. This electrode profile is expected to be satisfactory (as judged by the results obtained on this program) and advantageous for scaling to larger sizes because of the simplicity of its shape. The major difficulty with other electrode shapes, such as the Rogowskii profile, is the extreme width which must be used if the central portion of the electrode is made very planar to avoid constriction of the discharge width.

## 2. Aerosol Studies and Optical Measurements of Potassium

We observed in some of our previous work with small-scale apparatus (75 cm<sup>3</sup>) significant optical scattering losses in potassium-rare-gas mixtures at high temperatures (300°C) and pressures (10 atm). This was also found to be a problem with the large-volume apparatus shown in Figure III-5. Quantitative optical transmission measurements and qualitative side scattering observations were conducted during this study with apparatus of the type shown schematically in Figure III-7. Results of transmission measurements with a broadband tungsten light source are illustrated in Figure III-8. It is apparent from the data in Figure III-8 that a large optical loss

M11399

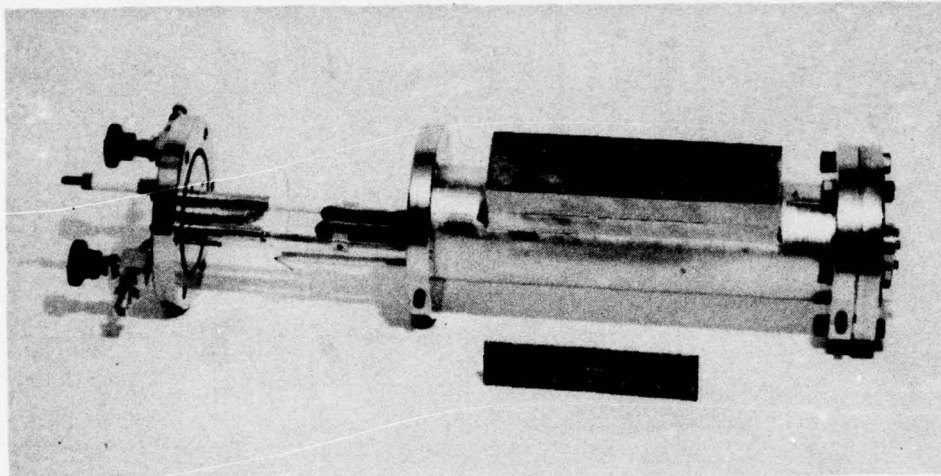


Figure III-5. Photograph of alkali-rare-gas high-pressure discharge apparatus, design 2.

M11595

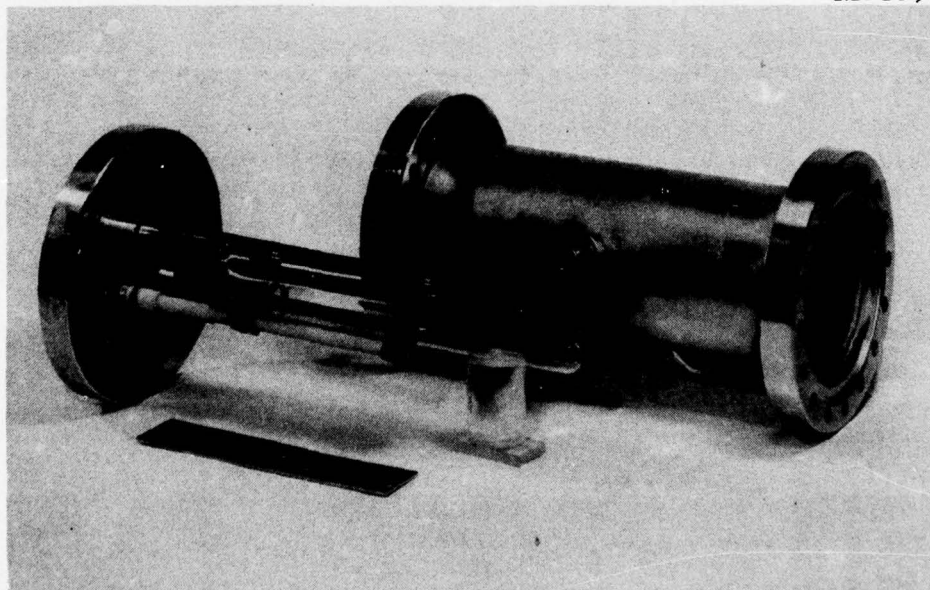


Figure III-6. Photograph of alkali-rare-gas discharge apparatus, design 3.



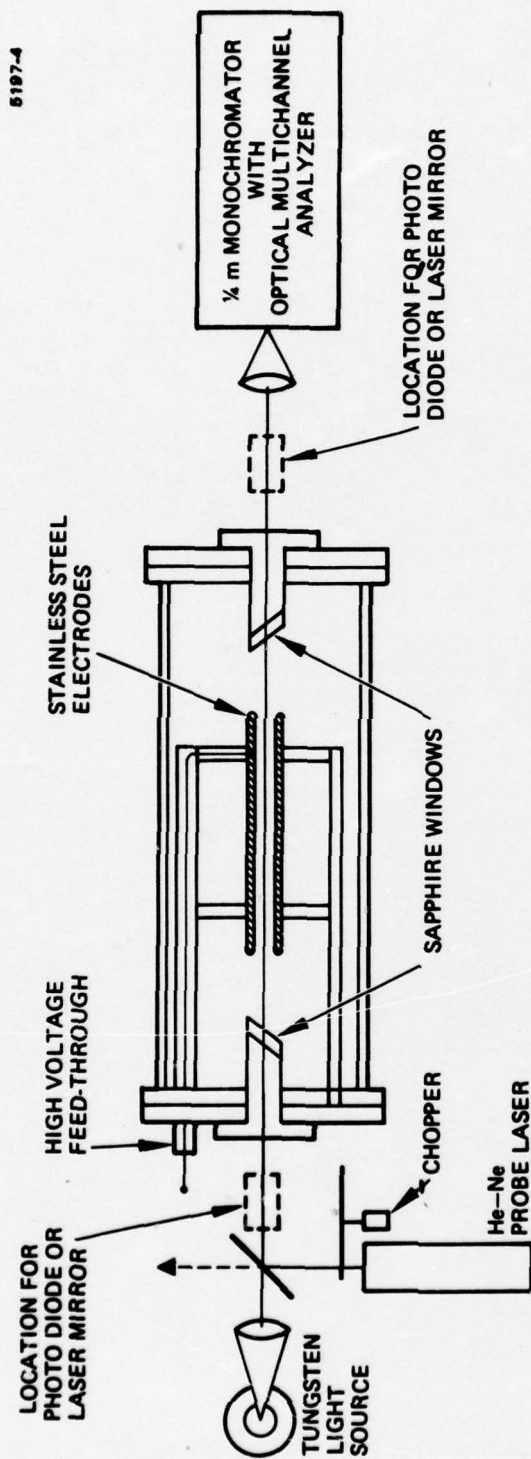


Figure III-7. Schematic of alkali-rare-gas discharge apparatus and optical monitoring equipment.

4854-2 R1

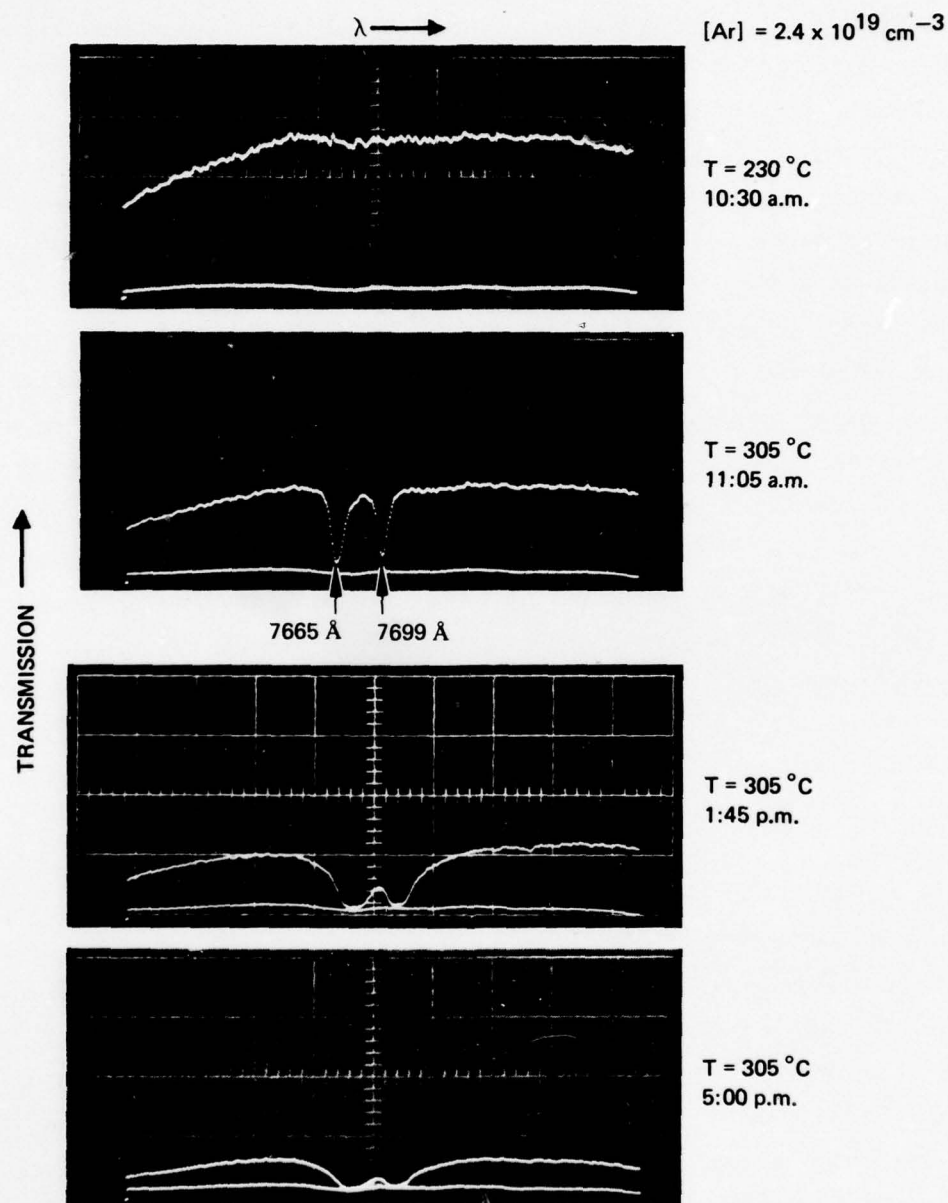


Figure III-8. Optical transmission data illustrating aerosol formation in potassium-argon mixture.

occurs over a wide wavelength region ( $\approx 400 \text{ \AA}$ ) under certain experimental conditions. In addition to this transmission reduction with time, strong side scattering from an He-Ne laser beam was also observed. This experiment was conducted with the apparatus shown in Figure III-5. Potassium was vaporized from a  $0.6 \times 15 \text{ cm}$  stainless-steel wick, located near the bottom of the housing, with an argon pressure of 1 atm. Following these observations of aerosol formation in the discharge apparatus, diagnostic experiments were conducted in sealed-off pyrex vessels located in a uniform-temperature muffle furnace, as shown in Figure III-9.

Optical transmission measurements with the broadband light source over  $400 \text{ \AA}$  bandwidths centered at  $7700 \text{ \AA}$  and  $6475 \text{ \AA}$  at different pressures of argon were carried out; transmission and scattering measurements with an He-Ne laser beam were also performed. The cell was filled with potassium and argon on a separate processing apparatus, sealed off, and located in the furnace for optical measurements. Quantitative correlations with equilibrium atomic potassium and potassium dimer densities were observed over the temperature range from  $25$  to  $350^\circ\text{C}$  and argon pressures from  $0$  to  $2 \text{ atm}$ ; experiments were not conducted at higher argon pressures in this apparatus. A comparison between our measured values of potassium dimer absorption coefficient and those of Lapp and Harris<sup>27</sup> is shown in Figure III-10. Combining their value of  $20 \text{ \AA}^2$  for the absorption cross section of  $\text{K}_2$  at  $6465 \text{ \AA}$  with our measured absorption coefficient of  $0.098 \text{ cm}^{-1}$  at  $325^\circ\text{C}$  yields a potassium dimer density of  $4.9 \times 10^{13} \text{ cm}^{-3}$ , which compares very favorably with the density of  $5.0 \times 10^{13} \text{ cm}^{-3}$  calculated from equilibrium vapor pressure data.<sup>28</sup> It is more difficult to deduce atomic densities of potassium from optical absorption measurements at high temperatures and pressures because of the complex optical broadening mechanisms involved; a well documented growth curve for the integrated absorption under these conditions has not been established. However, since we have obtained good agreement between equilibrium values of potassium dimer



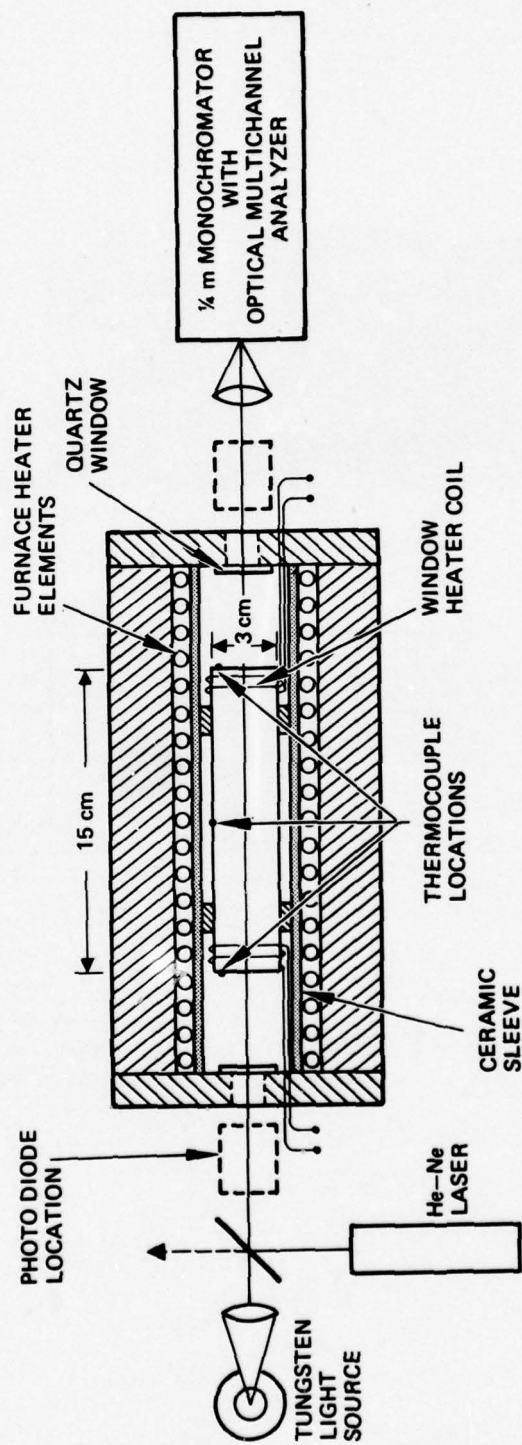


Figure III-9. Schematic of apparatus for optical measurements of alkali-rare-gas mixture with uniform temperature control.

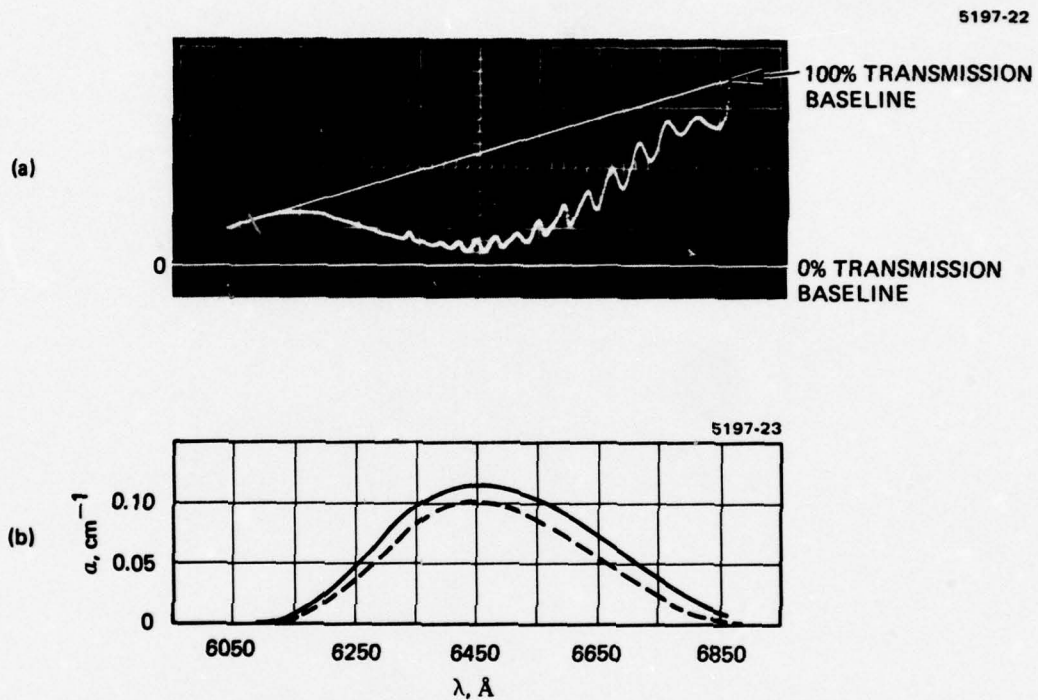


Figure III-10. Potassium dimer. (a) Optical transmission and (b) absorption coefficient. Solid curve is from Reference 27, dashed curve is our measurement.  $T = 325^\circ\text{C}$ ;  $L = 15 \text{ cm}$ ;  $P_{\text{Ar}} = 2 \text{ atm}$ .

densities and our measurements, it is reasonable to infer that an equilibrium between atomic and dimeric potassium is attained in our apparatus. Thus, we have obtained atomic potassium densities from measurements of dimeric potassium under conditions where the dimer spectrum is pressure broadened into a continuum.

Aerosol formation was not observed during the experiments conducted in this apparatus. This is illustrated by the optical transmission data shown in Figure III-11, which was obtained under the carefully controlled conditions described above. Note the dramatic contrast between this data and that shown previously in Figure III-8. We conclude that equilibrium values of potassium vapor density can be obtained in argon at temperatures up to  $350^{\circ}\text{C}$  and pressures up to 2 atm if the temperature of the apparatus is kept uniform. This is considerably more difficult in the discharge system, unless elaborate heating equipment is incorporated, because of the uneven heat capacity of the internal parts of the discharge chamber. We infer that potassium aerosols form when macroscopic-size volumes of saturated vapor densities come in contact with cold spots inside the discharge chamber. In the region around these cold spots, the saturated vapor density is transformed to a super-saturated vapor through heat transfer to the colder region. The super-saturated vapor is subsequently converted to an equilibrium vapor by condensation into macroscopic particles of liquid potassium. High pressures of inert gas in a large-diameter chamber contribute to aerosol formation by increasing the diffusion time of the alkali vapor and thereby preventing it from maintaining a dynamic equilibrium with the coldest regions in the chamber.

With this hypothesis and our experience with the sealed-off cells in the uniform oven, we postulated that aerosols could be eliminated in the large discharge apparatus by slowly evolving the potassium vapor in the absence of inert gas and then mixing pre-heated gas with the alkali vapor after equilibrium vapor densities of the pure metal vapor were obtained. Experiments were performed using this procedure by pre-heating argon to a temperature  $50^{\circ}\text{C}$  higher than the



POTASSIUM-ARGON  
 $\rho_A = 2.2 \times 10^{19} \text{ cm}^{-3}$

5008-1

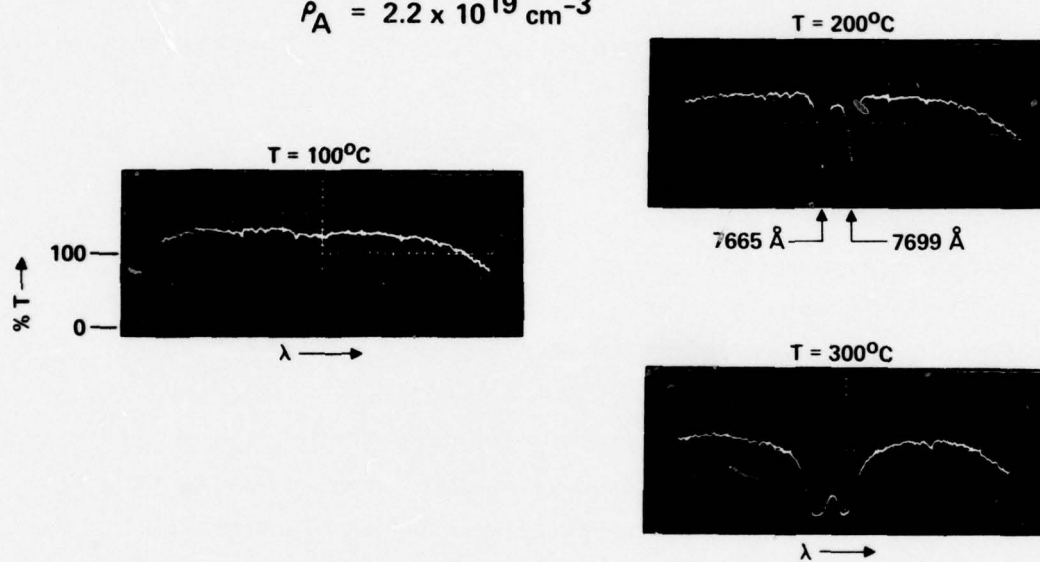


Figure III-11. Optical transmission through potassium-argon in a 15 cm sealed-off cell.

temperature of the discharge chamber. Uniform mixing was achieved by admitting the gas into the potassium vapor through a perforated stainless-steel sting. The results from these experiments are summarized by the optical transmission data in Figure III-12 (taken with the apparatus shown in Figure III-4). No aerosol formation occurred as indicated by this data and the complete absence of scattering from the He-Ne laser beam indicates the absence of aerosol formations. Thus, we arrived at an experimental procedure for obtaining homogeneous mixtures of alkali vapors and rare gases at high temperatures ( $300^{\circ}\text{C}$ ) and pressures (7 atm). These values of temperature and pressure are by no means expected to be upper limits; rather, they reflect the range over which carefully controlled experiments have been conducted in apparatus of the type necessary for alkali-rare-gas excimer laser systems.

Optical transmission data taken with the apparatus shown in Figure III-7 for two pressures of argon is given in Figure III-13 along with calculations from our theoretical model. The agreement between theoretical predictions and the experimental measurements is considered quite satisfactory and lends further support to the model.

### 3. Electrical Discharge Experiments

Electrical discharge measurements were carried out after establishing an aerosol-free mixture of potassium vapor and argon at 7 atm pressure. Using this argon density ( $9 \times 10^{19} \text{ cm}^{-3}$ ) and an oven temperature of  $300^{\circ}\text{C}$ , several experiments were conducted to evaluate both the electrical and optical characteristics of the discharge. Qualitative visual observations of the discharge through the 1.5 cm side viewing window and through the end windows indicated that a very uniform diffuse discharge over the entire electrode area was obtained without using any discharge preconditioning. This is partially illustrated by photographs of the discharge through the side window shown in Figure III-14. The field of view of the camera used is considerably smaller than the full discharge region and also smaller than

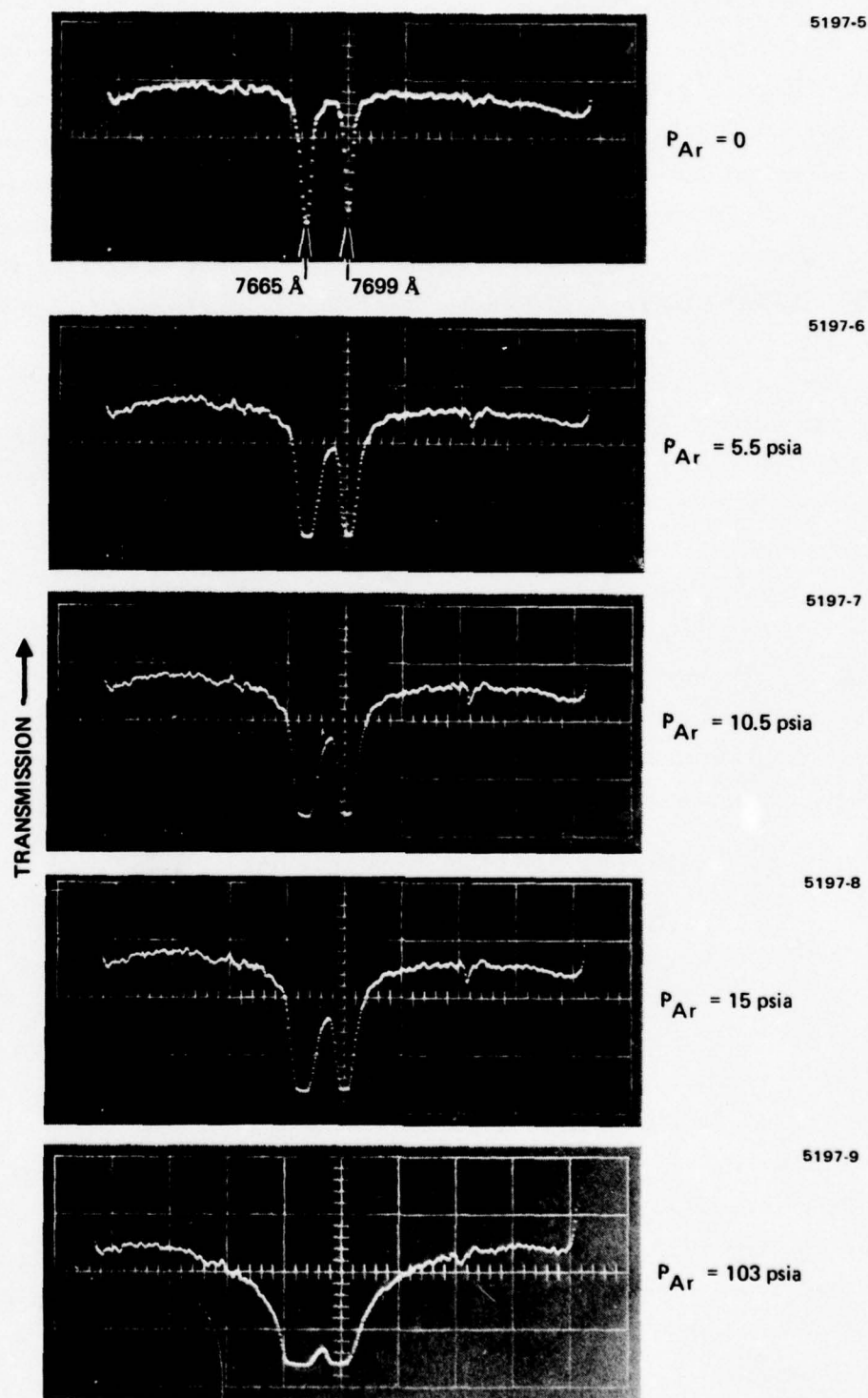


Figure III-12. Optical transmission through the discharge apparatus; no aerosol formation indicated ( $T = 300^{\circ}\text{C}$ ).



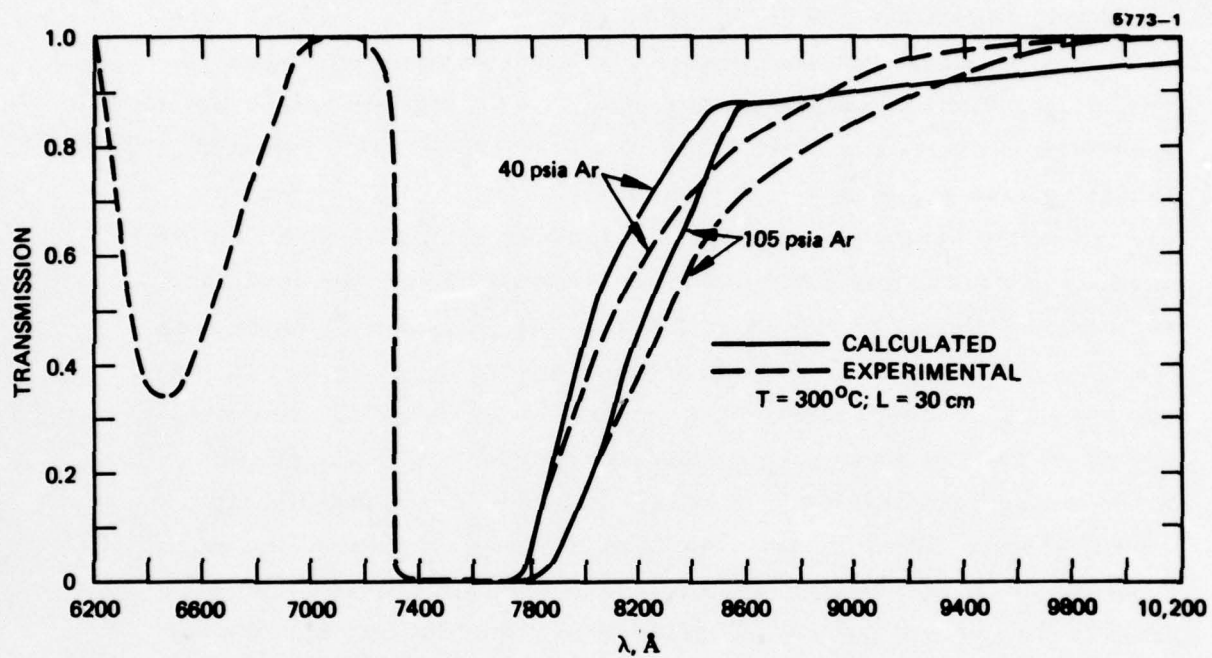


Figure III-13. Experimental and calculated optical transmission data for the configuration shown in Figure III-4 (K-Ar).

the field of view of a person's eye located adjacent to the side window. Two exposure levels are shown to verify the lack of small-scale striations in the discharge. As far as can be ascertained, the discharge is very uniform under the temperature and pressure operating conditions used here ( $300^{\circ}\text{C}$ , 7 atm argon).

Voltage and current characteristics of this pulsed discharge operating without preionization are shown in Figures III-15 and III-16. A negative voltage is applied across the electrodes with a thyatron switching tube and a capacitor previously charged to a particular voltage level. The current pulse develops after a delay time of a few microseconds and has a time duration dictated by the self-inductance and capacitance of the circuit rather than the plasma impedance. As the applied voltage is increased, breakdown occurs at earlier times and the peak current increases in proportion to the charge initially stored on the capacitor. This variation in time between application of the voltage and development of the current is not visible in Figures III-15 and III-16 because the complete time interval of the experiment cannot always be displayed on the time scale chosen to fully resolve the current pulses. Considerable power loading into the discharge has been achieved ( $\sim 10 \text{ kW/cm}^3$ ) without an arc developing. When the temperature is decreased by  $25^{\circ}\text{C}$  from the indicated temperature of  $300^{\circ}\text{C}$ , arcing does occur approximately 50% of the time and arcs were observed occasionally at voltages near 9 kV. A few experiments were also carried out using a quartz flashlamp for preionization of the discharge. The results have not been examined in detail, but it was noted that the time interval between discharge current onset and voltage application decreased markedly (several microseconds) as flashlamp intensity increased.

In addition to characterizing the electrical features of the discharge, we have also conducted spectroscopic investigations of the optical emission at wavelengths from  $7400 \text{ \AA}$  to  $1.1 \text{ }\mu\text{m}$ . An emission spectrum in the wavelength region near the potassium-argon excimer band is shown in Figure III-17(a). Self-absorption by ground-state

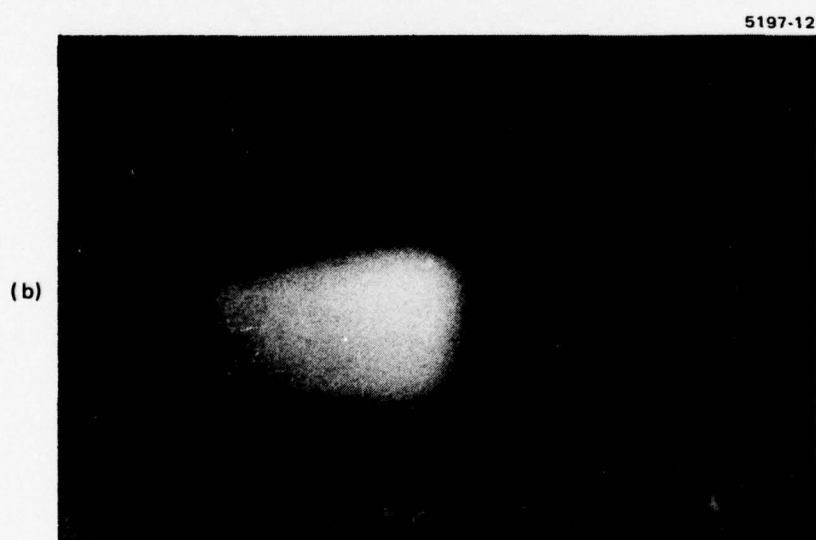


Figure III-14. Photograph of potassium-argon discharge as viewed through the 1.5 cm side window. Film exposure of (b) is 0.2 that of (a).



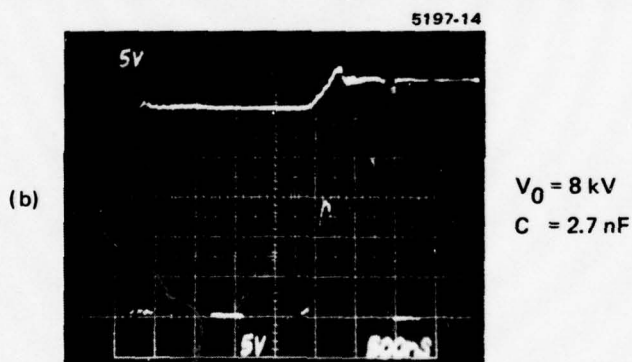
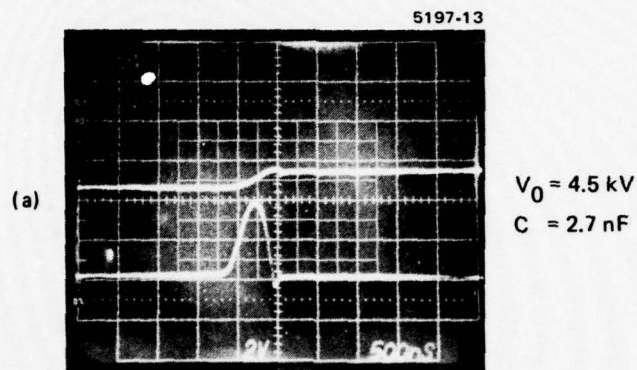


Figure III-15.  
 Current-voltage waveform characteristics  
 of potassium-argon transverse discharge.  
 Upper traces — voltage, lower traces —  
 current. Sensitivities: (a) 5 kV/cm,  
 20 A/cm; (b) 5 kV/cm, 50 A/cm.

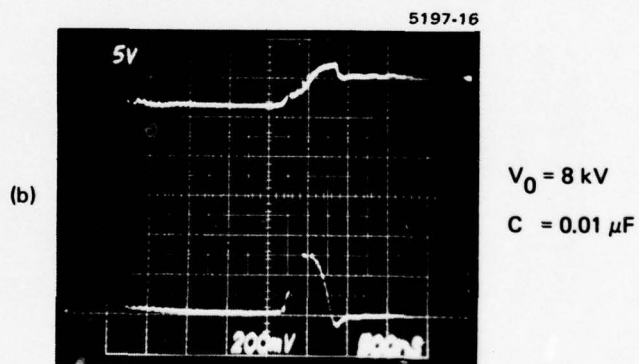
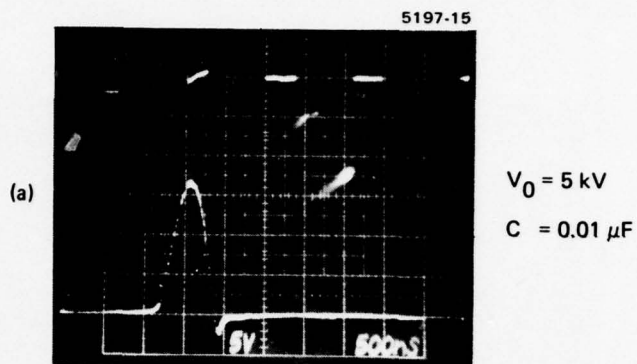


Figure III-16.  
 Current voltage characteristics of  
 potassium-argon discharge. Upper traces -  
 voltage, lower traces - current. Sensi-  
 tivities: (a) 5 kV/cm, 50 A/cm; (b) 5 kV/  
 cm, 200 A/cm.

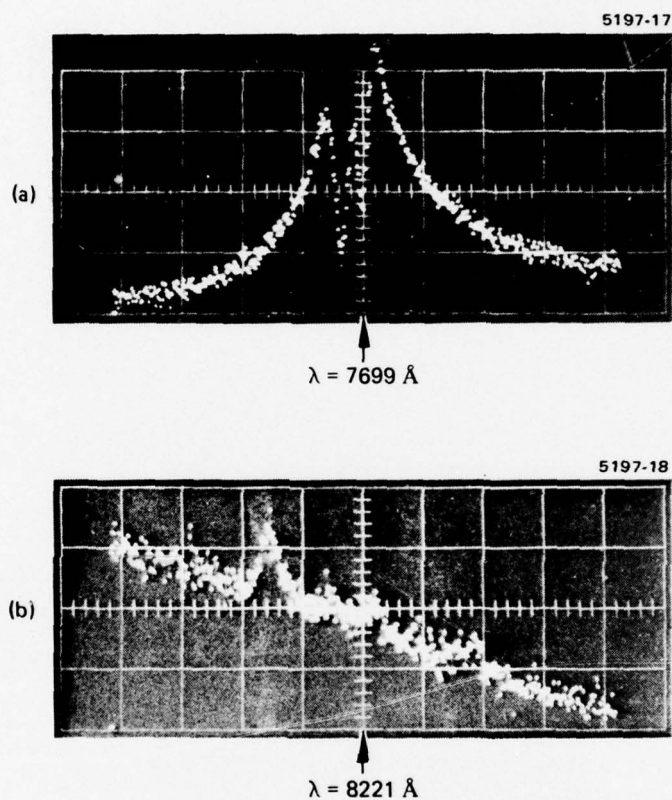


Figure III-17.  
Potassium-argon excimer emission. Sensitivity  
of (b) is 2.5 times that of (a). Wavelength  
scale —  $100 \text{ \AA/cm}$ .  $T = 300^\circ\text{C}$ ,  $P = 7 \text{ atm}$ ;  
 $0.01 \text{ }\mu\text{F}$ ,  $5.5 \text{ kV}$ .



potassium in the region between the electrodes and Brewster angle windows is responsible for the two negative peaks at 7665 and 7669 Å. The length of this optical loss region would be reduced from the present 5 cm to ~1 cm for an actual laser device. Another spectrum is shown in Figure III-17(b) with an intensity scale 2.5 times more sensitive than in Figure III-17(b), which demonstrates the large bandwidth and spectral shape of the excimer emission. The emission peak at 8085 Å has not been specifically identified, but may have resulted from impurities in the system. No discharge emission could be detected at wavelengths greater than 8700 Å with the OMA detection system, although strong potassium dimer emission is expected at 1.04 μm. This is consistent with the sharp falloff of silicon detector sensitivity in this spectral region; unfortunately, time did not permit a further spectral investigation with a more sensitive detector.

An additional experimental observation on the discharge emission, shown in Figure III-18, indicates that the excimer emission in the 7700 Å region closely follows the temporal behavior of the discharge current pulse. Figure III-19, which shows a comparison between potassium-argon excimer emission and absorption, illustrates (along with Figure III-17(b)) the extension of the long wavelength excimer emission beyond the absorption region. It is in this spectral region that the excimer emission is strong compared to absorption and, consequently, where optical gain can be obtained.

Although the contract period ended before quantitative emission studies could be properly carried out, we can make an estimate of the potassium resonance level population produced in the discharge from the data shown in Figure III-17. This emission was observed with the optical end-on configuration shown in Figure III-7, which is adequate for qualitative spectral data but is not optimum for obtaining quantitative results concerning excited-state populations. However, it is possible to make an estimate, and we have carried out an approximate evaluation of the potassium resonance level population by using a tungsten-iodine light source having a known spectral brightness. This

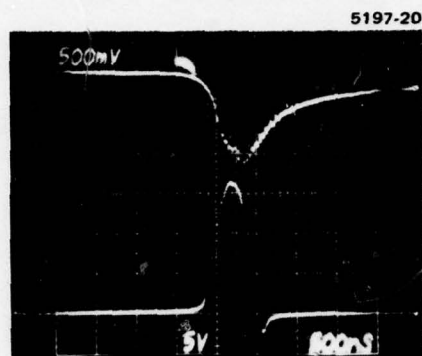


Figure III-18.  
Temporal profiles of  
potassium-argon excimer  
emission (upper trace) and  
discharge current (lower  
trace).

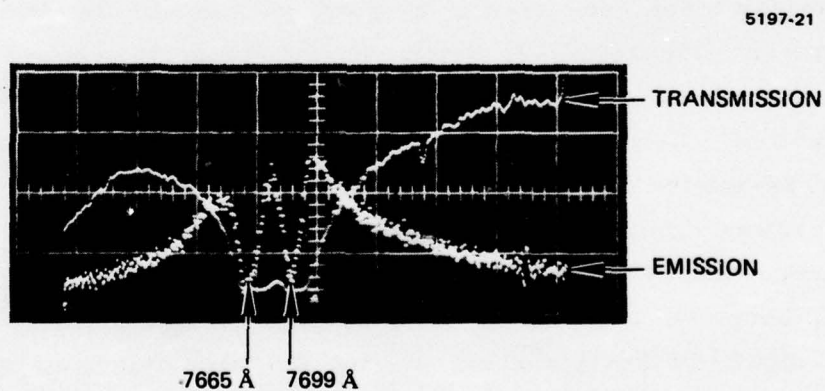


Figure III-19. Superposition of potassium-argon  
excimer optical emission and trans-  
mission spectra.

standard source was placed in the same location as the discharge electrodes shown in Figure III-7 so that the geometrical factors which influence the light flux passing through the optical system would be the same for both the standard source and the discharge emission. Obviously, this measurement could have been carried out more accurately by viewing the discharge and standard source from the side through apertures of optimum size and position. Nevertheless, an approximate evaluation of the data on hand at the time of contract termination is given below.

The spectral brightness of the discharge emission at a particular wavelength is related to the brightness of the standard source and the ratio of detector signals obtained from the two sources when they are located in equivalent geometrical configurations. Care was taken to fulfill this condition as completely as possible to provide the same monochromator filling factor and solid angle subtended by the collection optics for the two sources. Because of the high aspect ratio of the discharge and the end-on configuration employed, the results obtained are expected to have an absolute accuracy only within an order of magnitude.

The spectral brightness of the discharge emission is related to the brightness of the standard source and the ratio of detector signals obtained from the two sources by

$$B_F(\lambda) = B_S(\lambda) \frac{(E_F(\lambda)/T_F(\lambda) \tau_F)}{(E_S(\lambda)/T_S(\lambda) \tau_S)}, \quad (\text{III-9})$$

where

$B_S(\lambda) \equiv$  spectral brightness of standard source,  
watts/cm<sup>2</sup>-sr-Å

$E_F(\lambda) \equiv$  optical multichannel analyzer (OMA) output signal obtained from the discharge emission at wavelength,  $\lambda$



$E_S(\lambda) \equiv$  OMA signal obtained when the standard lamp is placed in the same geometrical configuration as the discharge (see Figure III-7)

$T_S(\lambda), T_F(\lambda) \equiv$  transmission of neutral density filters used with the standard source and discharge emission, respectively

$\tau_S, \tau_F \equiv$  exposure time of OMA to the optical signals from the standard source and the discharge emission, respectively.

Once the spectral brightness of the discharge emission,  $B_F(\lambda)$ , has been determined, it can be used to estimate the fluorescence power,  $P_F(\lambda)$ , of the emitting species:

$$P_F(\lambda) \text{ (watts/cm}^2\text{-}\mathring{\text{A}}) \approx 4\pi B_F(\lambda)/L \quad (\text{III-10})$$

where  $L$ , the pathlength of the emission region, is assumed to be optically thin. The concentration of emitting species is then related to fluorescence power by the expression

$$N(\text{cm}^{-3}) = P_F(\lambda) \Delta\lambda\phi\tau_o/h\nu, \quad (\text{III-11})$$

where  $\tau_o$  is the natural radiative lifetime of the emitting state (reciprocal of the Einstein A coefficient) and  $\phi$  is the quantum emission yield from this state;  $\phi$  is assumed to be unity.

In the case of excimer emission, many upper and lower states can combine to produce radiation at a particular wavelength, so  $\tau_o (\equiv 1/A)$  must be obtained from a summation over all the component substates of the upper and lower electronic states. This was carried out as described in Section III. A and Eq. (III-8), which gives relationships between the cross section for excimer and dimer emission at a particular wavelength,  $\sigma_S(\lambda)$ , and the Einstein A coefficient for the

potassium resonance levels. This yields an expression for the resonance level population,  $N_R$ , in terms of the measured spectral brightness of the discharge emission:

$$N_R(\text{cm}^{-3}) = k \lambda^5 P_F(\lambda) / \sigma_S(\lambda) \quad . \quad (\text{III-12})$$

For  $P_F(\lambda)$  in units of watts/cm<sup>3</sup>-Å,  $\sigma_S(\lambda)$  in cm<sup>2</sup>, and  $\lambda$  in Å,  $k = 4.2 \times 10^{-22}$ . Using the data shown in Figure III-17 and the previous expressions, we obtain the values of 0.034 watts/cm<sup>2</sup>-sr-Å, 0.031 watts/cm<sup>3</sup>-Å, and  $7 \times 10^{13}$  cm<sup>-3</sup> for the discharge emission brightness ( $\lambda = 8220$  Å), fluorescence power ( $\lambda = 8220$  Å), and resonance level population, respectively.

As shown in Figure II-3, the potassium excimer is not expected to show positive gain under these conditions ( $T \approx 300^\circ\text{C}$ ). However, the resonance level population deduced from the fluorescence power at 8200 Å can be combined with the stimulated emission coefficient,  $\sigma_S(\lambda)$  (calculated as described above), to yield a value for the gain coefficient of the potassium dimer on the satellite band at 1.04 μ:

$$g_o(\lambda) = \sigma_S(\lambda) N_R - \beta_A(\lambda) \quad . \quad (\text{III-13})$$

Using the value of  $N_R$  deduced above from emission measurements and the calculated values of  $0.3 \times 10^{-16}$  cm<sup>2</sup> and  $0.1 \times 10^{-2}$  cm<sup>-1</sup> for the stimulated emission cross section and absorption coefficient, respectively, we find that

$$g_o(1.04 \mu) \approx 0.1\%/\text{cm} \quad . \quad (\text{III-14})$$

This value for the gain at 1.04 μ is highly encouraging since it is large enough to support laser oscillation under attainable laboratory conditions and because it was obtained under experimental conditions that

are judged to be far from optimum. It is considerably lower than predicted from our theoretical modeling efforts, but this may be due to the experimental uncertainties discussed above. Additional experimental and theoretical studies are obviously required to fully evaluate the potential of discharge pumped potassium excimer and dimer laser systems.



#### IV. CONCLUSIONS AND RECOMMENDATIONS

We have shown theoretically that all of the A-X alkali-xenon excimer and the A-X alkali dimer transitions are feasible, broadband, high-efficiency average power laser transitions. Small-signal gain as a function of wavelength was computed for all of the alkali-xenon and alkali dimer transitions for flashlamp pumping; discharge characteristics and small-signal gain at the peak of the excimer and dimer gain band of the K-Xe and K-Ar systems were also computed for discharge pumping.

A probe laser measurement of the stimulated emission coefficient on the K-Xe excimer band at  $8220 \text{ \AA}$  obtained with flashlamp pumping is consistent with the theoretical modeling. In the discharge experiments, a diffuse discharge through a potassium-argon mixture was achieved at partial pressures and power loadings into the discharge which, according to the modeling, are sufficient to reach lasing threshold on both the excimer and dimer band with a 10 to 20 cm gain path. Although time did not permit definitive experimental confirmation of the discharge pumped laser gain, there were no indications that the physics of the laser excitation and emission processes are other than those considered in the theoretical studies. However, the recombination rate assumed in the modeling did lead to a discrepancy in the I-V characteristics between theory and experiment.

Because of the extensive effort required to develop methods and techniques for handling alkali metals at high temperatures and for suppressing aerosol formation at high pressures, it was not possible to spend sufficient time during this contract period on optimizing the discharge pumping technique. This technique was successfully developed and demonstrated during the last few months of the contract period. However, the experimental results which were obtained are highly encouraging and indicate that the potassium-rare-gas excimer/dimer discharge pumped laser system is worth further study.

In view of the scalability and efficiency predicted for discharge pumping and the experimental demonstration of a uniform glow discharge in a transverse configuration, it is recommended that this relatively simple pumping technique be given highest priority in furthering the feasibility demonstration of a high-energy alkali excimer/dimer laser system.

## V. ALKALI SOURCE STUDIES

An important consideration in developing alkali-rare-gas lasers is choosing an optimal technique for evolving the alkali vapor into the active column of the laser. During this program we have experimented with several alternative alkali source techniques and have given consideration to several others. A summary of what has been learned about each of these techniques follows.

### A. Cesium Chromate Pellets

This was one of the first alkali sources used in the program. Its use was motivated by a desire to avoid loading the alkali under sealed-off conditions. The cesium in the chromate pellets does not oxidize in air as it does in the free metallic form and, therefore, can be easily handled. The pellets are placed in a row along the tube, and once the tube is sealed off from the atmosphere, the alkali vapor is irreversibly released from the pellets by heating them with an electric current. The technique proved impractical for our experiments because the small amount of alkali released (on the order of a milligram) was inadequate to achieve equilibrium alkali vapor pressure within the tube volume.

### B. Heat Pipe Oven Techniques

The heat pipe oven techniques are at the opposite extreme from the chromate pellet source. In this method, 20 to 50 g of alkali must be loaded into the heat pipe oven to thoroughly wet the wick. Heat pipe oven alkali sources are described adequately in the literature<sup>29, 30</sup> and their theory of operation will not be repeated here. There are three primary reasons that heat pipe ovens were not used in the present program. First, it is necessary to use a large amount of alkali; this is incompatible with the "breadboard" type of experimentation



appropriate to this phase of the program, which requires numerous disassemblies of the laser tubes. Second, it is necessary in the conventional heat pipe configuration to radially surround the active volume with a wick; this is incompatible with transverse optical pumping. Third, there is the problem of the aerosol cloud which forms in the end region of the heat pipe when it is used at the high rare-gas pressures required for our experiments.

C. Alkali Metal Deposition along the Tube Wall

Alkali metal deposited along the tube wall was the technique used throughout most of the optical pumping program. A sealed-off ampoule of alkali metal was glassed onto the tube; the metal was released into the tube in a sealed-off condition by magnetically breaking off the ampoule tip. There is at least one important problem associated with using this technique. In the case of potassium, the metal does not appear to wet the alkali-resistant glass liners which are used for the internal wall of the tube. Eventually the potassium re-condenses into large isolated drops which ultimately obstruct the aperture of the tube. Also, it is not yet clear whether an alkali monolayer is formed uniformly enough along the remainder of the tube wall to ensure equilibrium alkali vapor pressures.

The technique currently being used to overcome the wetting problem described above is to deposit alkali metal along a strip wick of stainless-steel mesh. It is still not certain that equilibrium vapor conditions are obtained in this case.

D. Side Arm Evaporation

The technique used most commonly in the spectroscopy of alkali vapors is simply to evaporate the alkali in a vacuum from a side arm ampoule into the cell, thoroughly coating the cell walls with metallic alkali (except for the windows, on which condensation is avoided by keeping the windows at a slightly higher temperature).

This ensures attaining equilibrium vapor pressure when the cell is subsequently heated. This technique was used in discharge experiments where the tube walls do not have to have a high transparency.

E. Carrier Gas Transport of the Alkali

Ultimately, for high average power operation of an alkali-rare-gas laser, one will likely have to go to a flowing mixture. There are many years of magneto-hydrodynamic technology behind techniques for flowing alkali-rare-gas mixtures through a discharge which can be brought to bear on the problem at this stage. These techniques are well covered in the literature<sup>31, 32</sup> and need not be reproduced here.

## REFERENCES

1. A. V. Phelps, JILA Report No. 110, University of Colorado, 1972 (unpublished).
2. G. York and A. Gallagher, JILA Report No. 114, University of Colorado, 1974 (unpublished).
3. A. J. Palmer, J. Appl. Phys. 47, 3088 (1976).
4. A. J. Palmer and J. F. Fitzgerald, Second Summer Colloquium on Electronic Transition Lasers, Woods Hole, Mass. MIT Press, 1975.
5. R. E. M. Hodges, D. L. Drummond, and A. Gallagher, Phys. Rev. A 6, 1519 (1972).
6. Penetration of resonance lamp emission can be improved by operating the lamps at high pressure, as pointed out by D. L. Drummond, L. A. Schlie, and B. D. Guenther, Paper DA-5, 27th Gaseous Electronics Conference, Houston, Texas, 1974 (unpublished). However, alkali concentration in the laser mixture is still constrained to lower values than those which may be used under the present broadband optical pumping scheme.
7. A. J. Palmer, J. Appl. Phys. 41, 438 (1970).
8. R. M. Hill, D. J. Eckstrom, D. C. Lorents, and H. H. Nakano, Appl. Phys. Lett 23, 373 (1973).
9. J. Pascale and J. Vandeplanque, J. Chem. Phys. 60, 2278 (1974); CEA Reports, 1974 (unpublished).
10. P. P. Sorokin and J. R. Lankard, J. Chem. Phys. 55, 3810 (1971).
11. C. G. Carrington and A. Gallagher, J. Chem. Phys. 60, 3436 (1974).
12. J. Holstein, Phys. Rev. 72, 1212 (1947).
13. Handbook of Chemistry and Physics, 49th ed., edited by R. C. Weast (The Chemical Rubber Co., Cleveland, Ohio, 1968).



14. R. Scheps, Ch. Ottinger, G. York, and A. Gallagher, *J. Chem. Phys.* 63, 2581 (1975).
15. G. Herzberg, *Spectra of Diatomic Molecules* (Van Nostrand, New York, 1950), Appendix.
16. O. S. Heavens, *J. Opt. Soc. Am.* 51, 1058 (1961).
17. The A-state equilibrium constants are taken from Ref. 2 for Li, Na, and K with a temperature dependence assumed of the form  $\exp(D_A/T)$ , where  $D_A$  is the A-state dissociation energy. The values for Cs and Rb are estimated from scaling considerations.
18. Scaling arguments applied to measured recombination rates available, for example, in Ref. 12 are presented in Ref. 2 which indicate that the dimer A-state recombination rate constants for all of the alkali are on the order of  $8 \times 10^{-30} \text{ cm}^6 \text{ sec}^{-1}$ . Since the A-state population is not far from being in equilibrium with the resonance level population under the considered operating conditions, the computation results are not very sensitive to the exact value.
19. The g factors are obtained from the potential energy curves (Refs. 2, 9, and 15) and are the same for all of the alkalies except Cs where the Cs-Xe A-state degeneracy is chosen as 2. This is because the spin-orbit splitting of the  $6P_{1/2}$  and  $6P_{3/2}$  levels is large enough in this system to cause the respective A-X excimer bands to be separated by wavelengths which are comparable to the excimer gain bandwidth.
20. L. J. Kieffer, JILA Information Center Report No. 13, University of Colorado, Sept. 30, 1973.
21. Geoffrey V. Marr, *Photoionization Processes in Gases* (Academic Press, 1967).
22. S. C. Brown, *Basic Data of Plasma Physics* (The MIT Press, 1967).
23. G. York and A. Gallagher, JILA Report No. 114, University of Colorado, (Oct. 15, 1974).
24. R. E. M. Hodges, D. L. Drummond, and A. Gallagher, *Phys. Rev. A* 6, 1519 (1972).
25. A. von Engel, *Ionized Gases* (Oxford Clarendon Press, 1965).

26. J. V. Parker, R. R. Stephens and L. D. Hess, HF/DF Pulsed Chemical Laser Device, AFWL TR75-103 ARPA Order No. 1256, Contract F29601-73-C-0119.
27. M. Lapp and L. P. Harris, J. Quant. Spectrosc. Radiat. Transfer, 6, 169 (1966).
28. Thermodynamic Properties of the Elements, compiled by D. R. Stull and G. C. Sinke, Adv. Chem. Ser. No. 18 (1956).
29. C. R. Vidal and J. Cooper, J. Appl. Phys. 40, 3370 (1969).
30. C. R. Vidal and F. B. Haller, Rev. Scientific Inst. 42, 1779 (1971).
31. IEEE Proceedings 56, No. 9, Sept. 1968, a special issue on M. H. D. power generation.
32. M. Mitchner Partially Ionized Gases (Wiley, New York, 1973).

## APPENDIX

### COMPUTER PROGRAMS

Three computer programs are described in this appendix. Program OPUMPD computes the small-signal gain versus wavelength for broadband optical pumping of the alkali-rare-gas excimer/dimer systems for input values of rare gas concentration, gas temperature, and flashlamp flux. Subroutine program DIMER is required by OPUMPD and computes the optical pumping rate and stimulated emission and absorption coefficients versus wavelength for the dimer band from input conditions specified by OPUMPD.

Program KXECP takes as input the rare gas density, the oven temperature, the uv flux, and the voltage and capacitance of the discharge circuit and computes from the discharge model the discharge field; current density; electron density; alkali ion, excimer level, dimer level, alkali ground-state, and alkali resonance level concentrations; electron temperature; and the net gain and absorption coefficients at the peak of the excimer and dimer bands. These are all computed as a function of time. It can be interfaced with OPUMPD and DIMER if a gain versus wavelength output is desired for discharge pumping.

The flow diagrams (Figures A-1 through A-3) and listings for the programs are presented on the following pages. The OPUMPD and DIMER programs are written for the Honeywell G 635 time-sharing computer, and the KXECP program is written for the PDP10 computer.



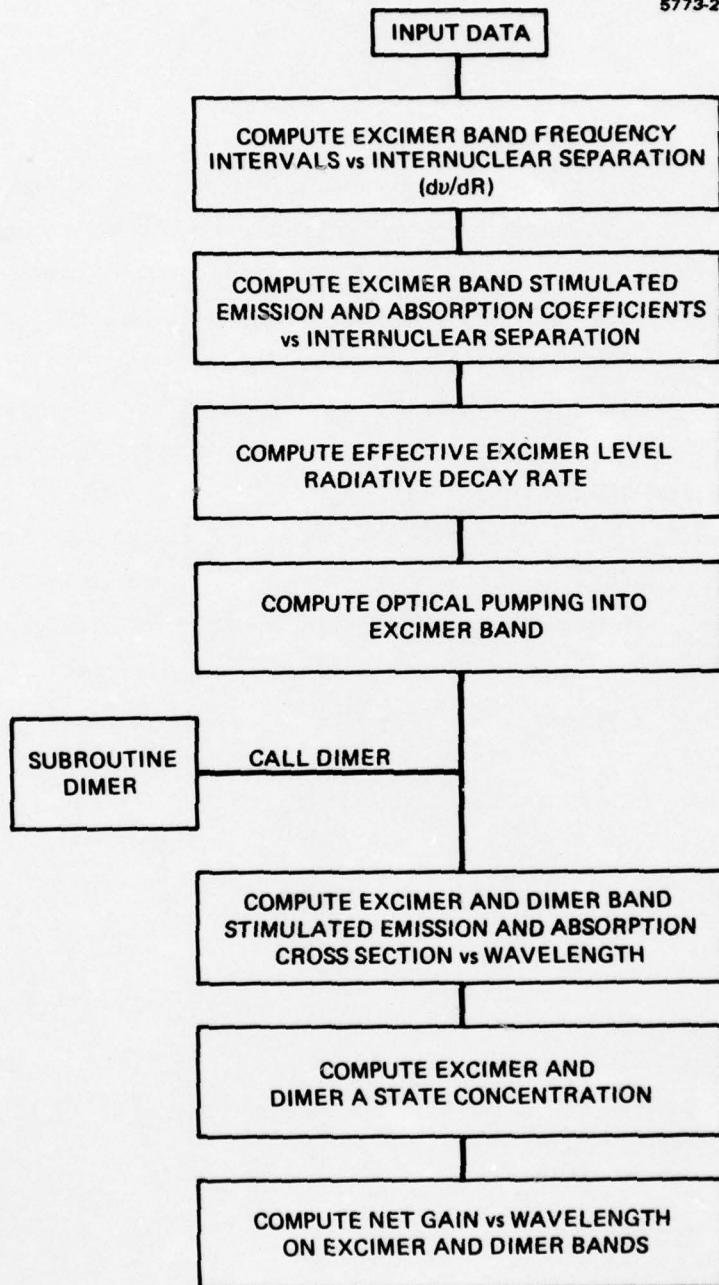


Figure A-1. Program OPUMPD.

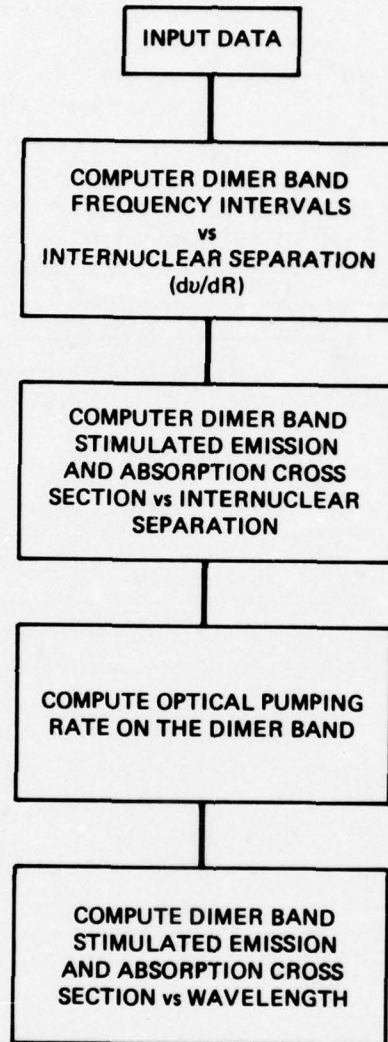


Figure A-2. Program DIMER.

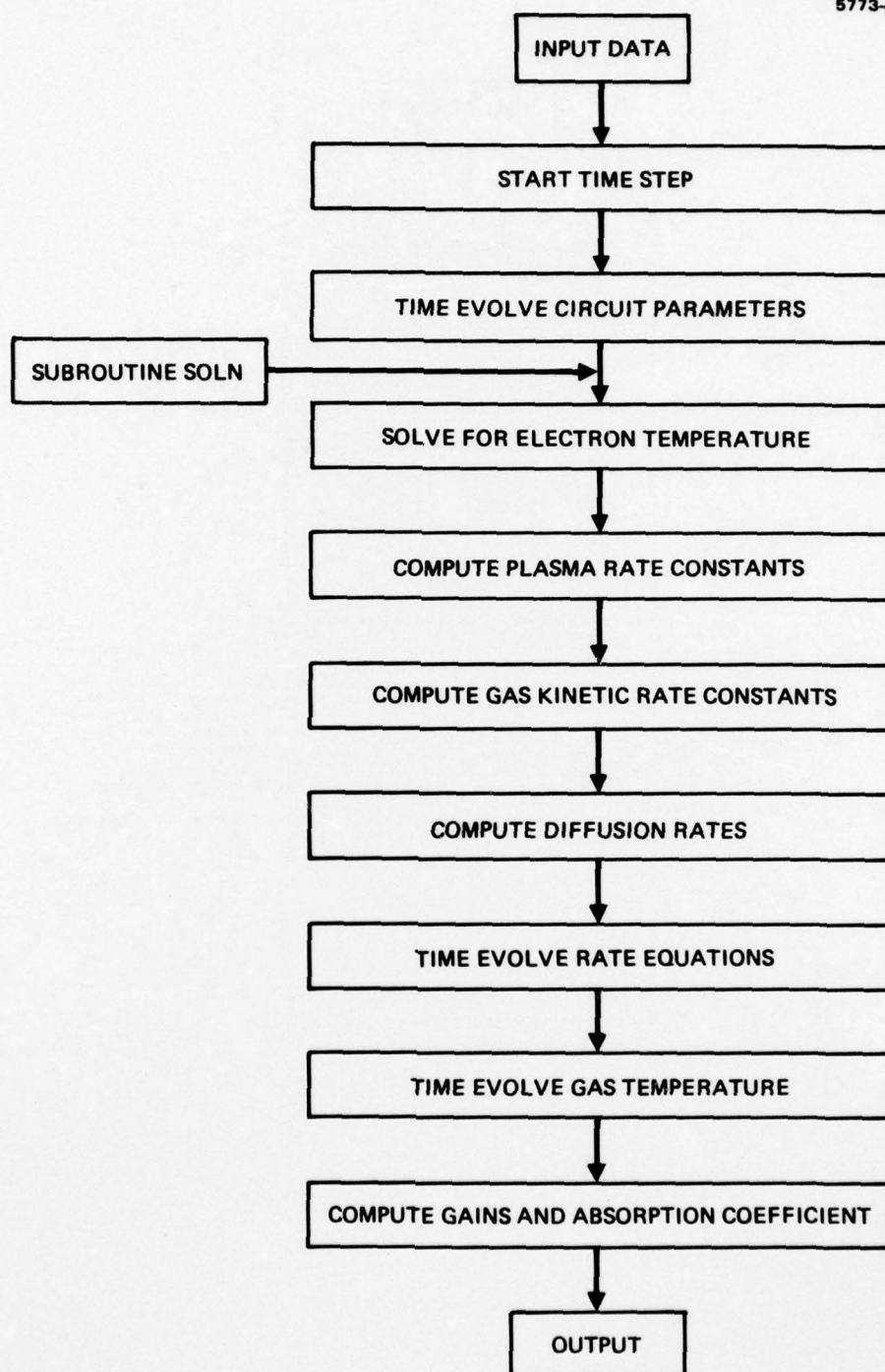


Figure A-3. Program KXECP.



```

5C PROGRAM OPUMPD - COMPUTES SMALL SIGNAL GAIN VS WAVELENGTH FOR ALKALI
6C XENON EXCIMER/DIMER SYSTEMS.  REQUIRES SUBROUTINE "DIMER".
7C
10 DIMENSION R(200),WU(200),WL(200),BET(200),
208 Dn(200),RWU(200),ALPH(200),RS(200),
308 LAMDA(30),ALPHA(30),BETA(30),GAIN(30),
328 WPU(27),WPL(27),ALPHD(30),BETAD(30)
45 DIMENSION BETT(200)
47 DIMENSION AT(200)
50 REAL LAMDA
52 REAL KE; REAL KD; REAL KEX; REAL NDI
53 REAL NR;REAL KEO;REAL KDO;REAL Mm
55C
60C DATA FOR K-XE
62 GU=4;GL=2;GR=6
64 GRD=12; GUD=1
70 NR=12.985E3
72 RO=30.
75 RZERO=5.
80 DF=170
90 FO=9.3E3
100 NUM=6
101 DEL=0.5/FLOAT(NUM)
102 NB=26*NUM
103 NBM=NB-1
105 DWR=.001E3/FLOAT(NUM)
110 AU=36.9E6
120 SA=8.4E4
130 SB=7.183
134 Mm=39.1
136 DA=5930
138 RE=8.2E-32
139 RD=8.E-30
140 DATA WPU/16.530E3,13.766E3,12.957E3,12.763E3,12.756E3,12.788E3,12.825E3,
1508 12.858E3,12.886E3,12.908E3,12.926E3,12.940E3,12.951E3,12.958E3,12.963E3,
1608 12.966E3,12.967E3,12.967E3,12.968E3,12.970E3,12.971E3,12.973E3,12.974E3,
1708 12.976E3,12.977E3,12.978E3,12.979E3/
205 KDO=6.5E-23
210 DATA WPL/5.431E3,2.235E3,1.053E3,0.558E3,0.306E3,0.158E3,0.066E3,0.009E3,
2208 -.022E3,-.037E3,-.042E3,-.042E3,-.038E3,-.033E3,-.028E3,-.023E3,-.019E3,
2308 -.016E3,-.013E3,-.010E3,-.008E3,-.007E3,-.006E3,-.005E3,-.004E3,-.003E3,
2408 -.003E3/
245C
250C ENERGY VS R INTERPOLATION
271 I=1
272 DO 520 J=1,NB
273 WU(J)=WPU(I)+(WPU(I+1)-WPU(I))*(J-NUM*(I-1))/NUM
274 WL(J)=WPL(I)+(WPL(I+1)-WPL(I))*(J-NUM*(I-1))/NUM
275 IF(J-NUM*(I-1)-NUM) 520,519,519
276 519 I=I+1
277 520 CONTINUE
278C
279C COMPUTE R(I)
281 DO 2 I=1,NB
290 R(I)=RZERO+FLOAT(I)*DEL
300 2 CONTINUE
304C
305C INPUT READ IN
310 PRINT:"ENTER RG"
320 READ: RG
330 PRINT:"ENTER TGO (DEG C)"
340 READ: TGO
350 ALK=2.7E16*((273/(273+TGO))*10**((SH-.052*SA/(TGO+273)))
360 PRINT:"ALK=",ALK
370 PRINT:"ENTER W (WATTS/(CM**2*MICRON))"
380 READ: W
385 PRINT:
390 X=1.
391C

```

```

392C CONVERT N TO PHOTONS/(CM**2*SEC*(CM)**-1)
400 F=N/(1.6E-19*1.55)*1E-4
404C
405C CONVERT TGO TO EV
410 TG=(TGO+2/3)*(1/1.16E4)
411C
412C COMPUTE RESONANCE LINE ABSORPTION COEFFICIENT
420 KU=KDO*EXP(DA*1.24E-4/TG)
430 BETR=ALK*AU/(8*3.14*NR**2*1E10)
431A *GU/GL
438C
439C COMPUTE FREQUENCY INTERVALS
442 DO 10 I=1,NBM
443  N=1
450 31 Dn(I)=(WU(I+K)-WL(I+K)-(WU(I)-WL(I))/FLOAT(K)
460 1F (FLOAT(K)*ABS(Dn(I))-DnR) 36,35,35
462 36 N=K+1
464 1F (I+K-NB) 37,37,38
466 37 GO TO 31
470 38 Dn(I)=DEL*(NR-(WU(I)-WL(I)))/(RO-R(I))
480 35 CONTINUE
487C
488C COMPUTE STIMULATED EMISSION FACTOR VS R
490 ALPH(I)=0.5*AU*R(I)**2*RG*(0.53E-8)**3/(WU(I)-WL(I))**2
500A *EXP((NR-WU(I))*1.24E-4/TG)*DEL*(1/3E10)/ABS(Dn(I))
501A *GU/GR
507C
508C COMPUTE ABSORPTION COEF VS R
510 BET(I)=(0.5*AU*R(I)**2*RG*(0.53E-8)**3*ALK/(WU(I)-WL(I))**2)*EXP(-WL(I)
520A *1.24E-4/TG)*DEL*(1/3E10)/ABS(Dn(I))
521A *GU/GL
530 1F (BET(I)-BETR) 8,9,9
540 9 BET(I)=BETR
542 8 CONTINUE
544 1F (BET(I)*X-3.) 130,130,131
546 130 AT(I)=AU ; GO TO 10
548 131 AT(I)=AU*1.6/(BET(I)*X*(3.14*ALOG(BET(I)*X))**.5)
550 10 CONTINUE
560 DO 60 I=1,NB
562 1F (BET(I)*X-0.1) 41,42,42
564 41 BETT(I)=BET(I) ; GO TO 60
570 42 DO 50 J=1,NBM
580 1F (WU(I)-WL(I)-(WU(J)-WL(J)+ABS(DW(J))/2.)) 51,51,50
590 51 1F (WU(I)-WL(I)-(WU(J)-WL(J)-ABS(DW(J))/2.)) 50,52,52
600 52 BETT(I)=BETT(I)+BET(J)
620 50 CONTINUE
625 60 CONTINUE
628C
629C COMPUTE TRAPPED RADIATIVE RATE
631 FR=0.;AAV=0.
632 DO 13 I=1,NBM
633 FR=FR+(GU/GR)*12.56*R(I)**2*RG*(.53E-8)**3*DEL*EXP((WR-WU(I))*1.24E-4/TG)
634 AAV=AAV+(GU/GR)*12.56*R(I)**2*RG*(.53E-8)**3*DEL*EXP((WR-WU(I))*1.24E-4
635A /TG)*AT(I)
636 1F (FR-1.) 13,620,620
637 620 GO TO 622
638 13 CONTINUE
639 622 PRINT:"FR=",FR;PRINT:"AT(NBM)/AU=",AT(NBM)/AU;PRINT:"AAV/AU=",AAV/AU
640C

```

```

641C COMPUTE OPTICAL PUMPING RATES
643 ROPT=0
644 RSE=0
650 DO 15 I=1,NBM
652 RS(I)=F*ALPH(I)*ABS(DW(I))*EXP(-BET(I)*X)
654 RSE=RSE+RS(I)
660 RNU(I)=F*BET(I)*ABS(DW(I))*EXP(-BET(I)*X)
670 ROPT=ROPT+RNU(I)
680 15 CONTINUE
690 PRINT:"ROPT=",ROPT
691 PRINT:"RSE=",RSE
692C
693C COMPUTE OPTICAL PUMPING BANDWIDTH
700 RMAX=0.
710 DO 72 I=1,NBM
720 IF (RNU(I+1)-RMAX) 71,72,73
730 73 RMAX=RNU(I+1)
740 71 CONTINUE
750 72 CONTINUE
760 DO 77 I=1,NB
770 IF (RNU(I)-RMAX/2.72) 76,77,78
780 78 M=I; GO TO 79
790 76 CONTINUE
800 77 CONTINUE
810 79 DO 82 I=M,NB
820 IF (RNU(I)-RMAX/2.72) 80,81,82
830 80 N=I; GO TO 83
840 81 CONTINUE
850 82 CONTINUE
860 83 CONTINUE
890 PRINT:"LAMDA(M)=",1./(NU(M)-NL(M))
891 PRINT:"LAMDA(N)=",1./(NU(N)-NL(N))
909C
910C COMPUTE STIM. EMISS. COEF. FACTOR & ABSORPTION COEFFICIENT VS WAVELENGTH
920 DO 20 I=1,25
930 ALPHA(I)=0.;BETA(I)=0.
940 FREQ=F0+DF*FLOAT(I-1)
950 LAMDA(I)=1/FREQ
960 DO 91 J=1,NBM
970 IF (FREQ-(NU(J)-NL(J)+ABS(DW(J)/2.))) 90,90,91
980 90 IF (FREQ-(NU(J)-NL(J)-ABS(DW(J)/2.))) 91,92,92
990 92 BETA(I)=BETA(I)+BET(J)
1000 ALPHA(I)=ALPHA(I)+ALPH(J)
1010 91 CONTINUE
1020 20 CONTINUE
1030 CALL DIMER(RG,TGO,W,DF,F0,ALPHD,BETAD,ROPTD,RSD)
1262 NR=(ROPT+ROPTD*(1-(AU+RSD)/(AU+RSD+RD*RG/KD)))/
1263 (AAV+RSE+(AU+RSD)*RD*RG*ALK/(AU+RSD+RD*RG/KD))
1265 NDI=(ROPTD+RD*RG*ALK*NR)/(AU+RD*RG/KD+RSD)
1267 PRINT:"NDI=",NDI
1268 PRINT:"NR=",NR
1270 PRINT 6
1280 6 FORMAT (2X,5HLAMDA,16X,4HGAIN,12X,4HBETA)
1281C
1282C COMPUTE NET GAIN AND ABSORPTION COEFFICIENTS VS WAVELENGTH
1290 DO 21 I=1,25
1300 GAIN(I)=(ALPHA(I)*NR+ALPHD(I)*NDI)-(BETA(I)+BETAD(I))
1310 PRINT 7, LAMDA(I),GAIN(I),BETA(I)+BETAD(I)
1320 7 FORMAT (1X,E13.6,6X,E10.3,6X,E10.3)
1340 21 CONTINUE
1350 STOP
1360 END

```

ready

\*



# LIST

```

1C SUBROUTINE DIMER - COMPUTES OPTICAL PUMPING RATE, STIMULATED EMISSION
2C FACTOR, AND ABSORPTION COEF. VS WAVELENGTH FOR ALKALI DIMER MOLECULE
3C FROM INPUT CONDITIONS FROM OPUMPD PROGRAM
4C
5 SUBROUTINE DIMER(RG,TGO,W,DF,FO,ALPHD,BETAD,ROPTD,RSD)
10 DIMENSION R(200),WU(200),WL(200),BET(200),
208 DW(200),RWU(200),ALPH(200),RS(200),
308 LAMDA (30),ALPHD(30),BETAD(30),
328 WPU(20),WPL(20)
50 REAL LAMDA
57 REAL KD; REAL KDO
59C
60C DATA FOR K-XE
62 GU=1.;GL=1.;GR=12.;GG=4.
70 NR=12.565E3
72 RO=30.
75 RZERO=6.
100 NUM=10
101 DEL=0.75/FLOAT(NUM)
102 NB=19*NUM
103 NBM=NB-1
105 DWR=1.E-3
110 AU=36.9E6
120 SA=8.49E4
130 SB=7.183
139 RD=8E-30
150 WA=69.1
160 WX=92.6
170 MU=19.488
180 DA=17530-11600
190 DX=4516
200 UAO=11600-4516
205 KDO=6.5E-23
210 UX0=-4516
220 REA=5.1E-8
230 REX=3.92E-8
240 BA=1.22E7*WA*SQR(MU/DA)
250 BX=1.22E7*WX*SQR(MU/DX)
278C
279C COMPUTE R(I) AND MORSE POTENTIALS
281 DO 2 I=1,NB
290 R(I)=RZERO+FLOAT(I)*DEL
292 WU(I)=DA*(1.-EXP(-BA*(R(I)*.53E-8-REA)))*2+UA0
294 WL(I)=DX*(1.-EXP(-BX*(R(I)*.53E-8-REX)))*2+UX0
300 2 CONTINUE
304C
305C INPUT READ IN
350 ALK=2.7E16*(273/(273+TGO))*10**(SB-.052*SA/(TGO+273))
390 X=1.
391C
392C CONVERT W TO PHOTONS/(CM**2*SEC*(CM)**-1)
400 F=W/(1.6E-19*1.55)*1E-4
404C
405C CONVERT TGO TO EV
410 TG=(TGO+273)*(1/1.16E4)
411C
412C COMPUTE RESONANCE LINE ABSORPTION COEFFICIENT
420 KD=KDO*EXP(DA*1.24E-4/TG)
430 BETR=ALK*AU/(8*3.14*NR**2*1E10)
4318 *GU/GL
438C

```

```

439C COMPUTE FREQUENCY INTERVALS
442 DO 10 I=1,NBM
445 K=1
450 31 DW(I)=(WU(I+K)-WL(I+K)-(WU(I)-WL(I)))/FLOAT(K)
460 IF (FLOAT(K)*ABS(DW(I))-DWR) 36,35,35
462 36 K=K+1
464 IF (I+K-NB) 37,37,38
466 37 GO TO 31
470 38 DW(I)=DEL*(WR-(WU(I)-WL(I)))/(RO-R(I))
480 35 CONTINUE
487C
488C COMPUTE STIMULATED EMISSION FACTOR VS R
490 ALPH(I)=0.5*AU*R(I)**2*(1/KD)*(0.53E-8)**3/(WU(I)-WL(I))**2
500& *EXP((WR-WU(I))*1.24E-4/TG)*DEL*(1/3E10)/ABS(DW(I))
505& *GU/GR
507C
508C COMPUTE ABSORPTION COEF VS R
510 BET(I)=(0.5*AU*R(I)**2*ALK*(0.53E-8)**3*ALK/(WU(I)-WL(I))**2)*EXP(-WL(I)
520& *1.24E-4/TG)*DEL*(1/3E10)/ABS(DW(I))
521& *GU/GG
530 IF (BET(I)-BETR) 10,9,9
540 9 BET(I)=BETR
550 10 CONTINUE
631C
632C COMPUTE OPTICAL PUMPING RATES
640 ROPT=0.
642 RSD=0
650 DO 15 I=1,NBM
652 RS(I)=F*ALPH(I)*ABS(DW(I))*EXP(-BET(I)*X)
654 RSD=RSD+RS(I)
660 RNU(I)=F*BET(I)*ABS(DW(I))*EXP(-BET(I)*X)
670 ROPT=ROPT+RNU(I)
680 15 CONTINUE
690 PRINT:"ROPTD=",ROPT
691 PRINT:"RSD=",RSD
692C
693C COMPUTE OPTICAL PUMPING BANDWIDTH
700 RMAX=0.
710 DO 72 I=1,NBM
720 IF (RNU(I+1)-RMAX) 71,72,73
730 73 RMAX=RNU(I+1)
740 71 CONTINUE
750 72 CONTINUE
760 DO 77 I=1,NB
770 IF (RNU(I)-RMAX/2.72) 76,77,78
780 78 M=I : GO TO 79
790 76 CONTINUE
800 77 CONTINUE
810 79 DO 82 I=M,NB
820 IF (RNU(I)-RMAX/2.72) 80,81,82
830 80 N=I : GO TO 83
840 81 CONTINUE
850 82 CONTINUE
860 83 CONTINUE
890 PRINT:"LAMDA(MD)=",1./(WU(M)-WL(M))
891 PRINT:"LAMDA(ND)=",1./(WU(N)-WL(N))
909C
910C COMPUTE STIM. EMISS. COEF. FACTOR & ABSORPTION COEFFICIENT VS WAVELENGTH
920 DO 20 I=1,25
930 ALPHD(I)=0.; BETAD(I)=0.
940 FREQ=F0+DF*FLOAT(I-1)
950 LAMDA(I)=1/FREQ
960 DO 91 J=1,NBM
970 IF (FREQ-(WU(J)-WL(J)+ABS(DW(J)/2.))) 90,90,91
980 90 IF (FREQ-(WU(J)-WL(J)-ABS(DW(J)/2.))) 91,92,92
990 92 BETAD(I)=BETAD(I)+BET(J)
1000 ALPHD(I)=ALPHD(I)+ALPH(J)
1010 91 CONTINUE
1020 20 CONTINUE
1030 ROPTD=ROPT
1040 RETURN
1050 END

```

```

C KXECF - PULSED K-XE LASER
  REAL MASE,MASXE,MASM,M1,M2,M1,K,K3X,K5X,K41,NEO,NE
  REAL LAMDE,LAMDD,KAEX,KADI,KXEX,KXDI
  REAL NEP
  REAL J
  REAL LENGTH
  REAL KPLUS,KNI,KEL
  REAL L
  EXTERNAL FUNC
  COMMON/STOR/XE,PO,CPI,CXI,NE,NEP,L,A,R,DT,E,
+ EPI,EX1,CEL,MASE,MASXE,V,LENGTH,PI,CPII,CPI,EPI
  COMMON/STE/TE
C CONSTANT DATA (DATA IS FOR K-XE)
  MASE=0.5E6; E=1.6E-19; MASXE=131*1840*.5E6
  R=0
  C=2.7E-9
  D=1
  A=27
  LAMDE=.85E-4
  LAMDD=1.04E-4
  AP=3.69E7
  REX=3.7E-8
  RDI=5.4E-8
  RDIE=4.4E-8
  DRDFE=.53E-8/(579)
  DRDFD=1E-8/(.04E4)
  DRDFDE=.4E-8/(1.388E3)
  VEA=-.079
  VEX=.062
  VDA=-.66
  VDX=-.262
  VDXE=-.560
  EPI=1.61
  EPI=4.34
  EPXI=1.46
  EPXI=4.19
  EPDI=1.46
  EPDI=4.19
  CPI=6E-15
  CPI=.5E-16
  CPII=5E-16
  CPHI=.05E-18
  CEL=5.5E-16
  CDIF=1E-15
  SA=8.49E4;SB=7.18
  LENGTH=1
  K=160E19

```



```

AX2=4E7;AP=3.69E7;AXED1=4E7
CSTME=AP/2*LAMDE**2*REX**2*DRDFE
CSTMD=AP/2*LAMDD**2*TDI**2*DRDFD
CSTMDE=AP/2*LAMDE**2*TDIE**2*DRDFDE

```

C INITIAL CONDITIONS

```

WRITE(5, 50)
50 FORMAT(2X,2HXE,2X,2HTG,2X,1HW,2X,1HV,2X,1HC,2X,2HDT,2X,6HIPRINT,
+2X,4HTMAX,2X,5HDELAY)
ACCEPT*,XE,TG,W,V,C,DT,IPRINT,TMAX,DELAY
PO=2.7E16*(273/(273+TG))*10**(SB-.052*SA/(TG+273))
TG=(TG+273)*(1/1.16E4)
TGO=TG
F=W/(1.6E-19*EPI)*(1.24/EPI-.2)
KXDI=1.8E-22*EXP(.56/TG)
KXEX=2.2E-23*EXP(-.05/TG)
PX=KXEX*PO*XE
PD=KXDI*PO**2
PX=KXEX*PO*XE
PI=F*CPHI*PO*DELAY
PI=10.*PI
AT=AP*1.6/(8.3E-15*PO*D)
IF(AT-AP) 18,17,17
17 AT=AP
18 CONTINUE
WRITE(5, 82) PO,PD,PI
82 FORMAT(2X,'PO=',E10.3,5X,'PD=',E10.3,5X,'PI=',E10.3)
WRITE(5, 80)
80 FORMAT(4X,4HTIME,6X,5HVDISC,5X,1HJ,9X,2HNE,8X,2HP1,
+8X,3HPX1,7X,3HPDI)
WRITE(5, 85)
85 FORMAT(7X,1HP,9X,2HP1,8X,5HGAIN,5X,5HGAIN,5X,5HBETAE,5X,5HBETAD,
+5X,2HTE)

```

C TIME STEP

```

20 ISTEP=ISTEP+1
T=T+DT
IF(T-TMAX) 21,21,22
21 CONTINUE

```

C CIRCUIT RESPONSE

```

P=PO-(PI+PI)
NE=PI
V=V-DT*J*A/C
IERR=0;IND=1;EPS=0.01
TE=SOL.(IND,FUNC,.1,5.,EPS,IERR)
IF(IERR) 1,2,1
1 WRITE(5,*) IERR;GO TO 30
STOP
2 CONTINUE

```

C RATE CONSTANTS - ELECTRONIC

VD=SQRT(2\*TE/MASXE)\*3E10  
 J=NE\*E\*VD  
 VDISC=V-R\*J\*A-L\*A\*E\*VD\*(NE-NEP)/DT  
 NEP=NE  
 RC=6.38E7\*(SQRT(2\*TE))\*\*3  
 RPI=RC\*EXP(-EPI/TE)\*(1+EPI/(2\*TE))\*(NE\*CPI)\*P  
 RPIB=RPI/P\*EXP(EPI/TE)\*PI\*.33  
 RPI=RFN(EPI)\*(NE\*CPI)\*P  
 RPII=RFN(EPI-EPI)\*(NE\*CPII)\*PI  
 RECP=PI\*2.28E-26\*NE\*TE\*\*(-4.39)\*NE  
 RECPX=3.3E-5\*TE\*\*(-.67)\*PXI\*NE  
 RECPD=3.3E-5\*TE\*\*(-.67)\*PDI\*NE

C RATE CONSTANTS - GAS KINETIC

SQRTG=SQRT(TG)  
 KAEX=2.2E-23\*EXP(.074/TG)  
 KADI=6.5E-23\*EXP(.735/TG)  
 KXEX=2.2E-23\*EXP(-.05/TG)  
 KXDI=1.8E-22\*EXP(.56/TG)  
 GPX=XE\*8E-32\*XE\*PI  
 GPXB=XE\*8E-32/KAEX  
 GPD=P\*(XE\*8E-30\*PI)  
 GPDB=(XE\*8E-30)/KADI  
 GPXI=(XE\*8E-32\*XE)\*PI  
 GPXIB=(XE\*8E-32\*PXI)/KAEX  
 GPDI=(XE\*8E-30\*P)\*PI  
 GPDIB=(XE\*8E-30\*PDI)/KADI

C DIFFUSION RATES

KPLUS=2E3\*(3E16/(XE))\*SQRT(.03/TG)  
 KEL=VD/(VDISC/LENGTH)  
 DXE=SQRT(2\*TG/MASXE)\*3E10/(3\*(XE)\*CDIF)\*(4.8/D)\*\*2  
 DAPOS=KPLUS\*TE\*(4.8/D)\*\*2  
 DP=DXE\*1.8

C RATE EQUATIONS

PI=PI+DT\*(RPI+RECP+RECPX+RECPD-RPIB-AP\*(PXI+PDI)-DP\*PI)  
 IF (PI/P-3\*EXP(-EPI/TE)) 8,9,9  
 9 PI=P\*3\*EXP(-EPI/TE)  
 8 CONTINUE  
 PX=KXEX\*P\*XE  
 PD=KXDI\*P\*\*2  
 PI=PI+DT\*(RPI+RPII+RP2I+GPN\*P+P\*CPHI\*F-RECP-RECPX-RECPD-DAPOS\*PI)  
 PXI=GPX/(GPXB+AP)  
 PXI=KAEX\*PI\*XE  
 PDI=GPD/(GPDB+AP)  
 PDI=KADI\*P\*PI

C GAS TEMPERATURE

TG=TG+DT\*(NE\*VD\*VDISC/LENGTH-(4.8/D)\*\*2\*K\*(TG-TG0))\*2/(3\*XE)

C GAIN

```

      BETAE=CSTME*2*P*XE*EXP(-VEX/TG)/3E10+CSTMDE*P**2*EXP(-VDXE/
+TG)*.25/3E10
      BETAD=CSTMD*P**2*EXP(-VDX/TG)*.25/3E10
      GAINE=CSTME*(PX1*EXP(-VEA/TG)/(KAEX*1.5)-2*P*XE*EXP(-VEX/TG))/3E10
+--CSTMDE*(P**2*EXP(-VDXE/TG)*.25)/3E10
      GAINDC=CSTMD*(PD1*EXP(-VDA/TG)/(KADI*12)-P**2*EXP(-VDX/TG)*.25)
+/3E10

```

C OUTPUT

```

      IF(ISTEP/IPRINT-FLOAT(ISTEP)/FLOAT(IPRINT)) 31,30,31
30  CONTINUE
      WRITE(5,*) TG
      WRITE(5,99) T,VDISC,J,NE,PI,PX1,PD1
90  FORMAT(7(E10.2))
      WRITE(5,95) P,PI,GAINE,GAINDC,BETAE,BETAD,TE
95  FORMAT(3X,7(E10.2))
31  CONTINUE
      GO TO 20
22  WRITE(5,200)
200 FORMAT(2X,19H>0, GO ON---<0, END)
      ACCEPT*,Z
      IF(Z) 41,41,42
42  WRITE(5,250)
250 FORMAT(2X,28HNEW VALUES: DT, TMAX, IPRINT, F)
      ACCEPT*,DT,TMAX,IPRINT,F
      ISTEP=0
      GO TO 20
      STOP
41  END
      FUNCTION FUNC(TE)
      REAL NE,MASE,MASXE,LENGTH,NEP,L
      COMMON/STOR/XE,PO,CPI,CX1,NE,NEP,L,A,R,DT,E,
+ EPI,EX1,CEL,MASE,MASXE,V,LENGTH,PI,CPII,CPI,EPI
      VD=SQRT(2*TE/MASXE)*3E10
      RC=6.38E7*(SQRT(2*TE))**3
      RPI=RC*EXP(-EPI/TE)*(1+EPI/(2*TE))*CPI*PO
      REL=(CEL*XE*SQRT(2*TE/MASE))*3E10*(2*MASE/MASXE)*TE
      FUNC=(V-R*A*E*NE*VD-L*A*E*VD*(NE-NEP)/DT)/LENGTH
+ -(1/VD)*(RPI*EPI+REL)
      RETURN;END
      FUNCTION RFN(Y)
      COMMON/STE/TE
      RFN=6.38E7*(SQRT(2*TE))**3*EXP(-Y/TE)*(1+Y/(2*TE))
      RETURN;END

```